A new strategy for modelling sonochemical reactors: Coupling of the non-linear Louisnard model with mass and heat transport equations with applications to cavitating viscous fluids

Quinten Goris, Ariana Bampouli, Mohammed Noorul Hussain, Olivier Louisnard, Georgios Stefanidis, Tom van Gerven

Ultrasonics Sonochemistry 112 (2025) 107114

Contents lists available at ScienceDirect

Ultrasonics Sonochemistry

journal homepage: www.elsevier.com/locate/ultson

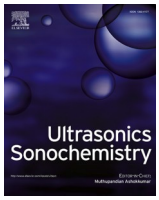

A new strategy for modelling sonochemical reactors: Coupling of the non-linear Louisnard model with mass and heat transport equations with applications to cavitating viscous fluids

Quinten Goris [a], Ariana Bampouli [a], Mohammed Noorul Hussain [a,1], Olivier Louisnard [b], Georgios D. Stefanidis [c], Tom Van Gerven [a,*]

[a] Department of Chemical Engineering, Process Engineering for Sustainable Systems, KU Leuven, Celestijnenlaan 200F, 3001 Heverlee, Belgium
[b] Centre RAPSODEE, IMT Mines-Albi, UMR CNRS 5302, Université de Toulouse, 81013 Albi CT, France
[c] School of Chemical Engineering, Department of Process Analysis and Plant Design, National Technical University of Athens, Iroon Polytecneiou 9, Zografou 15780, Athens, Greece

ARTICLE INFO

Keywords:
Acoustic cavitation
Bubble dynamics
Numerical simulation
Energy dissipation
Viscosity effect
Sonochemiluminescence

ABSTRACT

In this work, novel numerical models were developed and validated to offer new strategies in modelling sonochemical reactors. More specifically, in our original approach the non-linear *Louisnard* model was coupled with heat and mass transport equations to predict gradients in temperature and species concentration in a sonicated reactor. Additionally, a new operating window was investigated by modelling mixtures of increasing viscosity on both *micro-* and *macroscale* sonochemical effects. On the microscale, the effects of increasing viscosity on bubble dynamics were determined by solving the Keller-Miksis equation. Various cavitation threshold definitions were evaluated. The bubble collapse temperature was determined for all investigated mixtures and the energy dissipation of a single bubble was calculated. On the macroscale, different acoustic attenuation models were compared accounting for either linear or non-linear equations. Specifically, viscous losses were implemented in the non-linear *Louisnard* model, and model predictions were validated against experimental data. The model was able to predict multiple zones of cavitation in the reactor, as observed experimentally, and to estimate the dissipated energy for the different mixtures. Moreover, it was demonstrated that the cavitation-based attenuation dominates the other dissipation phenomena even for the most viscous solutions. The *Louisnard* model was coupled with heat transport equations, and using this extended version of the model, the temperature profiles were predicted for mixtures of increasing viscosity during sonication. Using a regression formula available in literature, radical production was related to the acoustic pressure field. By including reactions and mass transport in the acoustic model, for the first time in modelling ultrasonic reactors, the full distribution of light in the reactor during sonochemiluminescence (SCL) experiments for water was quantified.

1. Introduction: Modelling state-of-the-art

In recent years, the application of ultrasound to viscous systems, such as polymers [1–3] or food process streams [4] has shown to be promising. The main sonochemical improvements can be linked to the occurrence of acoustic cavitation, which involves the nucleation, expansion and violent collapse of microbubbles in the sonicated medium [5,6]. Provided the cavitation threshold pressure is exceeded, the bubble implosions are accompanied by hot-spot temperatures (>1000 K) and pressures (> 500 bar), free radicals, high shear stress, jetting streams and very localized velocity gradients [3,5–7]. Furthermore, gradients in the acoustic pressure field, possibly caused by cavitation, result in a net mean steady state flow, referred to as acoustic streaming [8,9]. On lab scale batch reactors, the application of ultrasonic energy has shown to improve both physical and chemical processing. Specifically, the combination of cavitation and acoustic streaming enhances both micro- and macromixing [10–12]. Therefore, to gain industrial relevance, a large cavitational zone should be achieved and maintained in the reactor [13]. However, the dynamic behavior and non-uniform distribution of cavitation bubbles hinder the successful prediction of sonochemical effects,

* Corresponding author.
E-mail address: tom.vangerven@kuleuven.be (T. Van Gerven).
[1] Current address: Department of Physics, University of Antwerp, Groenenborgerlaan 171, 2020 Antwerp, Belgium.

https://doi.org/10.1016/j.ultsonch.2024.107114
Received 17 September 2024; Received in revised form 14 October 2024; Accepted 15 October 2024
Available online 26 October 2024

preventing scale-up [5,6,14,15]. This challenge becomes more apparent for more viscous solutions commonly encountered in polymer synthesis, due to increased energy dissipation.

As acoustic energy dissipates, attenuation of the ultrasonic wave occurs, which limits the cavitation zone size in the reactor. In homogeneous media, classical thermoviscous attenuation mainly occurs via two mechanisms [16–19]. Firstly, viscous friction produces momentum diffusion, causing the dissipation of mechanical energy into heat. Secondly, heat conduction within the fluid is responsible for irreversible entropy production. At the same time, the presence of cavitation bubbles itself introduces a heterogeneity to the system, which leads to additional viscous and thermal attenuation terms superposed to the classical thermoviscous attenuation. In low-viscosity media, such as water, the cavitation-based attenuation is the dominant form of energy dissipation [20,21]. However, the investigation of the interplay between thermoviscous and cavitation-based attenuation in more viscous mixtures has not been conducted so far.

In the reviews of Sutkar & Gogate [5], and more recently Meroni et al. [6], various experimental techniques to map sonochemical activity are presented, including sonochemiluminescence (SCL), calorimetry, aluminum foil erosion, chemical dosimetry and particle image velocimetry (PIV). Nonetheless, experimental mapping might in some cases infeasible, time consuming, expensive, possibly intrusive and susceptible to uncertainties. Moreover, different techniques should ideally be combined in order to quantify the full sonochemical effects [5,14]. To gain additional knowledge, numerical models can be developed to predict the acoustic pressure field and corresponding sonochemical events [5,14,22,23].

Modelling ultrasound in a cavitating liquid is not trivial due to the high interdependency of the physical mechanisms involved, and the large variety of temporal and spatial scales on which they occur [6,14,24,25]. An overview of the latter phenomena can be found in Fig. 1. For a given vessel geometry and ultrasound source, an acoustic pressure field builds up in the reactor. The main difficulty arises from the coupling between the acoustic pressure field and acoustic cavitation [6]. When the acoustic pressure exceeds a threshold, gas pockets nucleate, grow, multiply and due to the Bjerknes forces, travel relative to the liquid. In parallel, the presence of cavitation bubbles introduces attenuation of the acoustic energy which modifies the acoustic pressure field. Moreover, the cavitation bubbles alter the sound speed spatially, resulting in wave dispersion [26,27], and the non-linear bubble oscillations also produce wave distortion [28,29]. The liquid medium itself also dissipates some acoustic energy via the classical thermoviscous mechanism, as previously explained. Lastly, acoustic streaming that results from amplitude gradients in the pressure field, can also exert drag forces on the cavitation bubbles, making their overall motion within the reactor complex [30–32]. Fully resolving the entire sonochemical coupling is cumbersome as it would require incorporating population balances for cavitation bubbles, which should be solved simultaneously with an equation for the pressure field and another for the acoustic streaming velocity [31,33]. Lesnik et al. [31] have performed such a simulation, but due to the high computation load they could only model a small part of a simple geometry.

Development of numerical models for acoustic attenuation constitutes an area of extensive research and has been mostly focused on the cavitation-based attenuation [26,34–36]. The first equations to model ultrasound fields in bubbly media were proposed by Van Wijngaarden [37,38] and were later more rigorously derived by Caflisch et al. [39]. However, Caflisch equations are computationally expensive and often fail to converge even for rather simple geometries [40]. Therefore, different authors have proposed simplifications to the Caflisch model as shown in Table 1. All strategies, with exception of the Westervelt model rely on solving either a linear or a non-linear Helmholtz equation in the frequency domain to obtain the acoustic pressure field.

The influence of the liquid viscosity on the sonochemical fields was investigated, mainly experimentally, in our previous work [23]. Specifically, custom mixtures of Polyethylene glycol (PEG) and water were utilized to increase the viscosity in a controlled manner. An experimental characterization campaign using calorimetry, sonochemiluminescence (SCL) and particle image velocimetry (PIV) was established. Additionally, a first simplified model was proposed for the prediction of acoustic cavitation zones [23]. However, the proposed rudimentary model required further extension and improvements.

Therefore, the present work aims to extend the *Louisnard model* in order to utilize its full potential to provide new strategies in modelling sonochemical reactors. A general overview of the manuscript contents can be found in Fig. 2. Firstly, a new operating window is examined by modelling sonochemical events in viscous fluids for both the *micro-* and *macroscale*. Secondly, additional physics are added to model heat transfer effects in a sonochemical reactor. The goal in this instance is to predict temperature gradients during sonication. Thirdly, chemical reactions (based on a regression formula) and mass transfer are included to model the luminol sonochemiluminescence reaction in water. This model strategy is proposed to fully capture the entire light distribution in the reactor during SCL experiments. The simulated results are validated against available experimental data. The coupling of heat and mass transport equations with an acoustic model is the first of its kind and allows to predict more accurately the effects of sonication in an ultrasonic reactor.

On the *microscale*, the influence of viscosity on the single bubble dynamics (cavitation threshold, hot-spot temperature and energy dissipated by an oscillating bubble) is examined. On the *macroscale*, the acoustic pressure field, total dissipated energy, acoustic streaming profiles and bubble pathways are calculated with respect to the medium viscosity. Special emphasis is placed on the influence of the viscosity on energy dissipation and different sound attenuation modelling theories

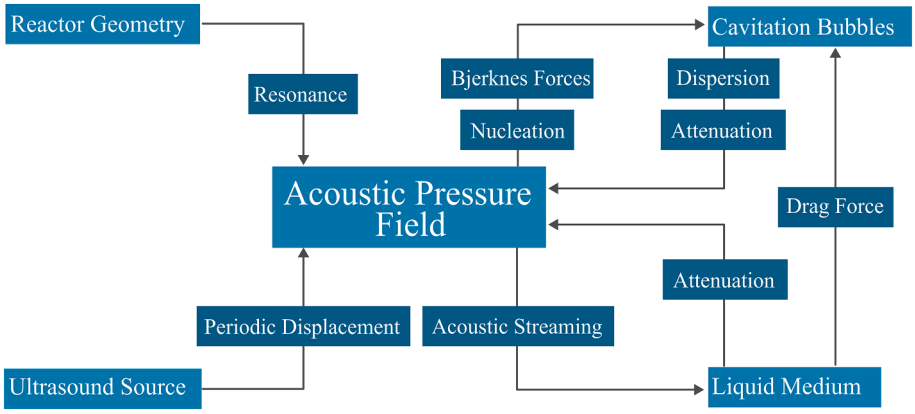

Fig. 1. Coupling between the physical mechanisms relevant in numerical modelling of sonochemical events, as identified in the scientific literature [24,25].

Table 1
Overview of the different modelling strategies for ultrasound propagation in bubbly liquids.

Model name	Type attenuation	Remark	References[1]
Linear models			
Linear Elastic (LE)	No Attenuation	Influence of attenuation omitted, resulting in overprediction of acoustic pressures.	[15,20,41–43]
Thermoviscous fluid model (TV)	Classical Thermoviscous	Inclusion of attenuation by appending fluid properties with complex valued terms.	[13,44–46]
Commander-Prosperetti (CP)	Cavitation-based[2]	Linearization of bubble dynamics which underpredicts the dissipation of energy. Still often applied in the scientific literature due to its simplicity.	[14,25,40,47–54]
Non-linear models			
Westervelt	Classical Thermoviscous	Used for high-frequency applications, where acoustic cavitation is not expected.	[55–58]
Louisnard (OL)	Cavitation-based	Imaginary part wavenumber derived from single bubble dynamics equations. Real part of the wavenumber calculated based on linear theory.	[22,26,30,47,59–62]
Trujillo	Cavitation-based	Both Imaginary and Real part of the wavenumber calculated based on single bubble dynamics.	[34,63,64]
Sojahrood	Cavitation-based	Both Imaginary and Real part of the wavenumber calculated based on single bubble dynamics.	[65–67]

Note[1]: Indicative references using the model, non-exhaustive list.
Note[2]: For the CP model the attenuation type could be considered bubble-based, since in theory it could be used for any type of bubbles if the size is not too large.

are compared. More specifically, the Linear Elastic model (LE), Thermoviscous fluid model (TV), Commander-Prosperetti model (CP) and Louisnard model (OL) are implemented and compared in terms of cavitation zone predictions. A comparison between the TV, CP and OL models was made to determine the most dominant dissipation mechanism for viscous solutions.

2. Experimental configurations

For the validation of the numerical simulations, the experimental set-up from our previous work [23] was modelled. This way the model could be validated against calorimetry, sonochemiluminescence (SCL) and particle image velocimetry (PIV) data. The following section provides a brief overview of the experimental setup and fluid properties.

The modelled reactor consists of a glass, double-jacketed cylinder with glass bottom and a capacity of 130 ml. Fig. 2 presents a schematic overview of the modelled experimental set-up and the dimensions of the reactor and transducer can be found in Table S1 and Table S2 of the Supporting Information. In the experiments, a Hielscher UP50H sonotrode transducer was used, which has an operating frequency of 30 ± 1 kHz and is rated for 50 W electrical power. An MS7 Titanium sonotrode was connected to the transducer inserted at a depth of 25 mm below the surface level of the reactor.

It is important to note that for this set-up sonotrode pulsations were observed experimentally for viscosities of $\mu = 123.2$ and $\mu = 712.5$ mPas [23]. For these configurations the sonotrode would require more electrical power than the safe power rating of the device, therefore the transducer switches to a pulse-like mode to protect its internal structures [23]. As this behavior is inherently transient, the pressure field, numerical dissipated power and streaming pathways cannot be solved since these result from steady state simulations. Since the temperature profiles in the reactor rely on the acoustic simulations also no accurate predictions can be made.

Therefore, in this work, for viscosities larger than 123.2 mPas, only microscale simulations of the bubble dynamics are presented. For completeness the acoustic pressure field, numerical dissipated power, streaming pathways and temperature profiles are presented in Section D of the Supporting Information. Results presented therein should be considered critically, since the simulations were performed as if the sonotrode was continuously operating and the model predictions could not be validated against experiments.

The viscosity of the investigated solutions was increased in a controlled manner by creating mixtures of PEG and water. All PEG-water mixtures had been carefully characterized in terms of viscosity (μ), density (ρ), speed of sound (c), surface tension (σ) and specific heat capacity (c_p). A more elaborate discussion on the measurement protocols can be found in our earlier work [23] and the exact values of the fluid properties are tabulated in Table S3 of the Supporting Information.

3. Numerical section

3.1. Resolving the microscale effects of the viscosity on the bubble dynamics

3.1.1. Bubble size

To calculate the single cavitation bubble dynamics, the ambient bubble radius R_0 needed to be known. Often the value of R_0 varies significantly in the literature and it is often used as a fitting factor, ranging from 1 μm up to 130 μm [23]. In this work, we used reported experimental data to more rigorously estimate R_0. However, since experimental data for a frequency of 30 kHz are scarce, bubble size distributions measured for 20 kHz were used. Measurements of Mettin et al. [32] indicate an ambient bubble size distribution between 1 and 10 μm with an arithmetic mean around 2 μm, which is confirmed by experiments of Burdin et al. [68] that measured a rather similar bubble distribution. The volume mean size of this distribution amounts to approximately 5 μm. Therefore, in all models, monodisperse bubbles were assumed with a single bubble size of $R_0 = 5$ μm. The choice for the volume mean size instead of the arithmetic mean was based on the Caflisch equations for bubbly liquids [39] where the bubble sizes enters the mass conservation equation as the derivative of bubble volume to time.

It should be noted that using the linear resonance size rule is not appropriate since it would yield ambient bubble radii larger than 100 μm for both 20 and 30 kHz, which does not correspond to the experimental results for active cavitation bubbles. When bubbles are too large, they experience shape instability followed by fragmentation, which limits the size range of cavitation bubbles. Intensive GPU based

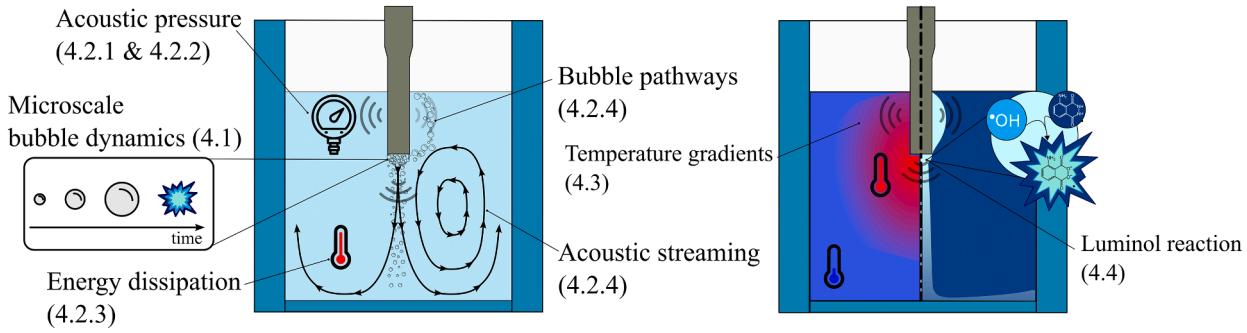

Fig. 2. General overview of the manuscript contents. The microscale is resolved by modelling viscosity effects on the single bubble dynamics. The macroscale simulations address the predictions of acoustic pressure, overall energy dissipation and acoustic streaming together with bubble pathways. Additionally, transport phenomena are included by modelling the heat transfer effects in a sonochemical reactor and the luminol sonochemiluminescence reaction.

numerical simulations performed by Klapcsik and Hegedüs [69] indicate that the medium viscosity increases the bubble shape stability, which prevents break-up. As a result, larger bubble radii can be anticipated for more viscous solutions. This comes in agreement with analytical results derived by Hilgenfeldt et al. [70,71]. In theory, using this GPU method, a range of stable nuclei could be predicted, however, this would require significant numerical resources and time [69]. Therefore, as mentioned before, in the current work an ambient bubble radius of 5 μm was used for all the mixtures as a simplification.

3.1.2. Single bubble dynamics

In a next step, the influence of the liquid viscosity on the bubble dynamics of a single oscillating bubble was determined. Here, bubble dynamics were computed by solving a system of coupled ordinary differential equations (ODE's). The same equations as in the work of Louisnard et al. were used [22,26,61]. Similar to the work of Toegel et al., the system of ODE's consists of three main parts: (1) a Keller-Miksis equation for the bubble radial motion, (2) conservation of the bubble content energy and (3) mass transport phenomena (including diffusion, condensation and evaporation of water) [72]. Details and derivations of the equations used in this study can be found in Section B.1 of the Supporting Information.

It should be noted that in the presented bubble dynamics calculations, no chemical reactions are directly taken into account as this would substantially increase the complexity. As an example, more than 20 reactions (excluding backwards reactions) need to be taken into account for a bubble containing only pure O_2 and water [73]. For an air–water bubble, simulations are reported including up to 93 reaction terms [74,75]. Moreover, some controversy was recently raised about the correct way to model chemical reactions in cavitation bubbles [76]. Recently, Hegedüs et al. proposed a regression formula to estimate the amount of $OH^{\bullet}$ radicals in function of the local acoustic pressure acting on a single bubble [73].

3.1.3. Cavitation threshold

A cavitation threshold above which bubbles undergo inertial oscillations should be defined for two purposes. Firstly, cavitation-based attenuation models require the knowledge of bubbly regions where the damping terms become active. Secondly, only those regions above the threshold pressure, can be reasonably thought as bubble-populated, which allows to predict the cavitation zones in the reactor, and to display bubble streams following the Bjerknes force field [61].

Several approaches for the cavitation threshold estimation exist in the scientific literature, with four cases standing out:

- The *Blake threshold* pressure (Eqs. (1) and (2)), separates small-amplitude quasistatic oscillations constrained by surface tension from large amplitude inertia-dominated oscillations [71,77,78]. It is interesting to note that this threshold is viscosity-independent.

$$p_{blake} = p_{\infty}\left(1 + \left(\frac{4}{27}\frac{S^3}{1+S}\right)^{\frac{1}{2}}\right) \tag{1}$$

$$S = \frac{2\sigma}{p_{\infty}R_0} \tag{2}$$

- The *Expansion Ratio (ER) threshold*, the pressure where $ER = \frac{R_{max}-R_0}{R_0}$ is equal or larger than two [69,73,79–81]. Variants of this threshold exist but they all rely on $\frac{R_{max}}{R_0}$, which is the maximum bubble expansion ratio over an acoustic cycle.
- The pressure amplitude at which the collapse temperature exceeds a certain cut-off value, herein named the T_{max} *threshold* [75,78,79]. Values for the cut-off collapse temperatures can range from 1000 K up to 5500 K [78]. The motivation for this threshold is that radicals production can be reasonably thought to increase with the collapse temperature. In this work, both a temperature cut-off of 3000 K and 5500 K were investigated. Radical production is of prime importance in the comparison of modelling results with those of SCL, which results from the reaction of luminol with sonochemically produced $OH^{\bullet}$ radicals.
- The pressure amplitude at which the bubble wall velocity upon collapse exceeds the speed of sound in the liquid, termed as *Mach threshold* hereafter [14,49,71,80]. It has been argued that a supersonic collapse would facilitate sufficient energy transfer to the gaseous bubble contents [70,71].

Using the computed bubble dynamics, each threshold based on the four different approaches was calculated and compared for the custom-made PEG-water mixtures.

3.1.4. Energy dissipation of single cavitation bubbles

Knowing the time-dependent bubble radius $R(t)$, the average energies, both thermal (Π_{th}) and viscous (Π_v), dissipated over an acoustic cycle (τ) due to a single cavitation bubble were calculated using Eqs. (3) and (4) [26,34,82]. Additionally, radiation energy losses (Π_{rad}) due to the compressibility of the liquid around the bubbles can be calculated. However, recently there has been some debate on the different attributions of viscous and thermal effects on the contribution of Π_v, Π_{th} and Π_{rad}. Therefore, in this work a more classical approach was adopted solely focusing on Π_v and Π_{th}, as originally derived by *Louisnard* [26].

$$\Pi_v = \frac{1}{\tau}\int_0^{\tau} 16\pi\mu R\left(\frac{\partial R}{\partial t}\right)^2 dt \tag{3}$$

$$\Pi_{th} = \frac{1}{\tau}\int_0^{\tau} -\frac{4\pi p_g}{3}\frac{\partial R^3}{\partial t} dt \tag{4}$$

3.2. Modelling the macroscale events of viscosity in a sonochemical reactor

3.2.1. Pressure field: Theoretical background on sound attenuation models and comparison

All considered models of attenuated sound waves start from the Helmholtz wave equation in the frequency domain:

$$\nabla^2 P + k_m^2 P = 0 \tag{5}$$

In Eq. (5), P is the acoustic pressure amplitude and k_m is the (modified) wavenumber, whose imaginary part represents the attenuation coefficient, $\alpha = -Im(k_m)$.

For the sonicated liquid, all the models presented herein were implemented via the *Pressure acoustics* module in COMSOL and were compared by determining the relative cavitation zone size, calculated as volume larger than the cavitation threshold divided by the total volume. Since the frequency of the sonotrode can vary between 31 and 29 kHz, simulations were performed for three different driving frequencies (29, 30 and 31 kHz).

3.2.1.1. Linear elastic model (LE). In the ideal, lossless case the squared wavenumber is defined as the square of the ratio of the angular driving frequency ω and the speed of sound of the medium c, as shown in Eq. (6). In this case k_{LE}^2 is real.

$$k_{LE}^2 = \left(\frac{\omega}{c}\right)^2 \tag{6}$$

3.2.1.2. Thermoviscous attenuation model (TV). In the classical thermoviscous attenuation model, the squared effective wavenumber k_{TV}^2 is defined by Eq. (7) [19].

$$k_{TV}^2 = k_{LE}^2(1 - i\epsilon_v) \tag{7}$$

where the dimensionless parameter ϵ_v is given by:

$$\epsilon_v = \frac{\omega}{\rho c^2}\left(\frac{4}{3}\mu + \mu_b\right) \tag{8}$$

In this equation, ω is the angular driving frequency, ρ is the density, c is the sound speed of the liquid. The bulk viscosity μ_b was assumed equal to the dynamic shear viscosity μ [23], although more recent research has indicated that the bulk viscosity can be up to a factor of 3 higher [83]. The dimensionless number ϵ_v is of the order of the ratio of the mean free path to the wavelength, and is therefore small in the present case, even for the most viscous liquid. The corresponding thermoviscous attenuation coefficient is defined by [18,19]:

$$\alpha_{TV} = \frac{k_{LE}}{2}\epsilon_v = \frac{\omega^2}{(2\rho c^3)}\left(\frac{4}{3}\mu + \mu_b\right) \tag{9}$$

3.2.1.3. Commander-Prosperetti model (CP). The Commander-Prosperetti model was employed to model the interaction of cavitation bubbles with the sound field in a linear way [36]. For a monodisperse bubble distribution the squared Commander-Prosperetti wavenumber (k_{CP}^2) is defined in Eq. (10).

$$k_{CP}^2 = \left(\frac{\omega}{c}\right)^2 + \frac{4\pi\omega^2 n_b R_0}{\omega_0^2 - \omega^2 + 2ib_{CP}\omega} \tag{10}$$

The linear resonance frequency of the bubbles ω_0 and the damping coefficient b_{CP} were calculated using the equations in Table S4 of the Supporting Information. The bubbles were assumed here to be filled mostly with air, hence the thermal diffusivity inside the bubble (D) and the ratio of specific heats for air (γ) were defined as $D = 21.9{\cdot}10^{-6}\frac{m^2}{s}$ and $\gamma = 1.4$, respectively [84].

The number of bubbles (n_b) in the second term of Eq. (10) is related to the volume fraction of bubbles (β) via Eq. (11). If the local acoustic pressure is lower than the cavitation threshold (p_{thresh}), no cavitation bubbles are present. Hence, $n_b = 0$ for $|P| < p_{thresh}$.

$$\beta = \frac{4\pi}{3} n_b R_0^3 \tag{11}$$

As previously highlighted [23], the value used for n_b (or in other words β) differs significantly between scientific publications and is not easily measured. Therefore in this work a parametric sweep is performed on n_b in order to obtain the best match with experimental validation data (SCL and calorimetry).

3.2.1.4. Louisnard model (OL). The non-linearity in the Louisnard model appears in the dependency of the wavenumber (k_{OL}^2) to the acoustic pressure amplitude $|P|$. Moreover, the imaginary part of k_{OL}^2, which is related to energy dissipation and attenuation, is calculated based on the bubble dynamics (Eqs. (3) and (4)) [22,26]. This way, in contrast to the Commander-Prosperetti theory, the non-linear bubble oscillations are accounted for. In the work of Louisnard, it has been reported that the viscous losses (Π_v) dominate the thermal losses (Π_{th}) [22,26]. Therefore in the current work only the viscous losses were accounted for in the wavenumber. The real and imaginary parts of k_{OL}^2 are calculated using Eqs. (12) and (13).

$$Re\left(k_{OL}^2\right) = \left(\frac{\omega}{c}\right)^2 + \frac{4\pi n_b R_0 \omega^2}{\omega_0^2 - \omega^2} \tag{12}$$

$$Im\left(k_{OL}^2\right) = -2n_b\rho\omega\frac{\Pi_v(|P|)}{|P|^2} \tag{13}$$

It should be noted that the real part of k_{OL}^2 is calculated based on the linear dispersion theory, in contrast to the more advanced models of Trujillo [34,64] and Sojahrood [82]. However, it has been postulated that the imaginary part dominates the squared wavenumber [26].

The number of bubbles (n_b) was set and fitted to obtain the best match with experimental data. Following the approach of references [22,26,30,61], the viscous dissipation function (Eq. (3)) was precalculated numerically by the bubble dynamics equations, non-dimensionalized and used in the non-linear COMSOL model. Similar to the Commander-Prosperetti models, $n_b = 0$ for $|P| < p_{thresh}$.

3.2.2. Comparing thermoviscous and cavitation-based dissipation

Whenever losses were included in the model, the mean total dissipated power in the liquid was calculated using Eq. (14) [85–87].

$$P_{diss,tot} = \iiint_V \frac{-Im\left(k^2\right)|P|^2}{2\rho\omega}\, dV \tag{14}$$

Evaluation of predicted dissipated power from the solutions of both the TV, CP and OL models allowed to investigate (1) the influence of linearization on the cavitation-based attenuation, (2) the relative importance of cavitation-based attenuation compared to thermoviscous attenuation, and (3) comparisons between model predictions of dissipated power and experimental calorimetry for the same set-up [23].

Additionally, the net energy flowing across the solid boundaries was quantified using Eq. (15) [85], where $\vec{n}$ denotes the unit normal vector pointing inward the liquid. In any case, conservation of mechanical energy requires that $P_{boundary} = P_{diss,tot}$.

$$P_{boundary} = \iint_S \frac{1}{2} Re\left(P\vec{U}_1^*\right)\cdot\vec{n}\, dS \tag{15}$$

The amplitude of the primary acoustic velocity field $\vec{U}_1$ was determined in function of the acoustic pressure amplitude P as shown in Eq. (16). The asterisk is used to denote the complex conjugate value.

$$\vec{U}_1 = \frac{i}{\rho\omega}\nabla P \tag{16}$$

3.2.3. Solid mechanics coupling with the acoustic pressure field

Using the COMSOL Solid mechanics module, the displacement of the sonotrode was determined. An overview of all the relevant equations can be found in the COMSOL Structural Mechanics Module user guide [88]. The sonotrode is composed of titanium and was modelled as an isotropic linear elastic material. The Young's Modulus, Poisson's ratio and density were taken as $E = 119$ GPa, $\nu = 0.33$ and $\rho = 4420$ kg/m^3, respectively. The solid mechanics were solved in parallel with the pressure field of the liquid, using a COMSOL acoustic-structure boundary Multiphysics coupling.

3.2.4. Acoustic streaming profile & bubble pathways

The acoustic streaming model originates from the perturbation theory of the Navier-Stokes equations [8,89]. Based on the work of Lighthill [8], it has been shown that the acoustic streaming can be predicted relatively well by solving the stationary Navier-Stokes equations with the inclusion of an acoustic driving force term (F) and a $\kappa - \epsilon$ turbulence model [30].

The driving force was calculated by taking the divergence tensor of the dyadic product of the primary acoustic velocity field $\vec{u}_1(\vec{r},t)$ shown in Eq. (17) [8,30,46,89].

$$\vec{F} = -\nabla\left(\rho\left\langle \vec{u}_1 \otimes \vec{u}_1 \right\rangle\right) \tag{17}$$

Using the identity $\langle f(\vec{r},t)g(\vec{r},t)\rangle = \frac{1}{2}Re(F(\vec{r})G^*(\vec{r}))$, the driving force can be expressed in function of the complex harmonic velocity field $U_1(\vec{r})$ and its complex conjugate (denoted by an asterisk), shown in Eq. (18).

$$F_i = -\frac{\partial\left(\rho\langle u_{1i}u_{1j}\rangle\right)}{\partial x_j} = -\frac{\partial\left(\rho\frac{1}{2}Re\left(U_{1i}U_{1j}^*\right)\right)}{\partial x_j} \tag{18}$$

As shown in Fig. 1 of the introduction, coupling between the acoustic field, the acoustic streaming and the cavitation bubbles leads to translational motion. Fully resolving the complete coupling would require significant computational power and remains highly complex [31]. Therefore in the current model a one-way coupling was implemented: in a first step the acoustic field and streaming velocity were computed, making abstraction of the bubble movement, and in a second step the bubble pathways were calculated qualitatively based on the terminal velocity.

The primary Bjerknes forces ($\vec{F}_b$) were calculated following the approach of reference [61], based on the bubble dynamics, the amplitude and phase of the acoustic pressure field. Next, the bubble mean translational velocity $\langle\vec{v}\rangle_\infty$ was determined using Eq. (19) [30].

$$\langle\vec{v}\rangle_\infty = \vec{u}_{strm} + \frac{\vec{F}_b}{12\pi\langle R\rangle\mu} \tag{19}$$

The streaming velocity $\vec{u}_{strm}$ was calculated from the Navier-Stokes equations and the average bubble radius over an oscillation period $\langle R\rangle$ was extracted from the bubble dynamics. As highlighted in reference [30], several debatable assumptions were made to obtain the above equation, and this issue deserves deeper investigations [90–92]. However, Eq. (19) allows a quick estimation of the bubble translations and has allowed to reproduce realistic phenomena [30].

3.3. Coupling the acoustic calculations with heat transport

Once the power dissipated in the sonicated medium was known (Section 3.2.2), an estimate of the temperature field in the sonochemical reactor could be made. Previously reported calorimetric experiments [23] were used for validation. The COMSOL *Heat transfer* module [93] was used, which solves the energy balance in a flowing fluid shown in Eq. (20).

$$\rho c_p\frac{\partial T}{\partial t} + \rho c_p\,\vec{u}_{strm}\cdot\nabla T - k_{cond}\nabla T = Q_{gen} \tag{20}$$

In this equation, k_{cond} is the thermal conductivity, c_p is the specific heat constant (experimentally measured for all mixtures) and Q_{gen} presents any local heat source. The latter is coupled to the acoustic field, as the dissipated acoustic power and was calculated based on the imaginary part of the wavenumber of the OL model to account for cavitation-based dissipation (Eq. (21)).

$$Q_{gen} = \frac{-Im\left(k_{OL}^2\right)|P|^2}{2\rho\omega} \tag{21}$$

The convective heat transfer relies on the acoustic streaming velocity ($\vec{u}_{strm}$) which was calculated at a constant temperature of 23 °C. In general, for simplicity all properties were evaluated at the initial temperature $T_{ref} = 23$ °C. Moreover, due to a lack of experimental data, the thermal conductivity for water ($k_{cond} = 0.598\frac{W}{m\cdot K}$ [94]) was used for all mixtures, however, for pure PEG400 a thermal conductivity in the order of $k_{cond} = 0.2 - 0.3\frac{W}{m\cdot K}$ has been reported [95]. Using the steady state acoustic pressure and acoustic streaming fields, the temperature profile in the reactor was calculated theoretically.

3.4. Coupling the acoustic calculations with reactions and mass transport

In a last stage, an effort was made to fully simulate experimental sonochemiluminescence (SCL) images. Often a cavitation zone under the horn tip is visible, followed by a streak of faint light emissions. The reason for this streak remains unclear but it can be reasonable to assume the delay time during SCL light emission combined with the acoustic streaming velocities might induce dispersion of light into the reactor. To test this hypothesis, the COMSOL *Transport of diluted species interface* was used to visualize how photons distribute into the reactor.

Sonochemiluminescence originates from luminol reacting with the sonochemically produced OH$^\bullet$ radicals. A complex reaction pathway is followed and in the last step excited reaction products emit blue/white light [21,96]. In the *Transport of diluted species* interface, the convection–diffusion equation is solved, including chemical reactions as shown in Eq. (22). More details on the specific COMSOL module can be found in reference [97]. The diffusion coefficient of the *OH*$^\bullet$ radicals in water was taken equal to $2.8{\cdot}10^{-9}$ m/s^2 [98,99].

$$\frac{\partial c_i}{\partial t} + \nabla\cdot\left(\vec{u}_{strm}c_i\right) - D_i\nabla^2 c_i = R(c_i) \tag{22}$$

In this equation, c_i is the concentration of species i, D_i is the diffusion coefficient and $R_i(c_i)$ is the rate of consumption/generation of species i, which in this case is coupled to the acoustic field. As for heat transfer, the convective transfer contribution is based on the acoustic streaming field $\vec{u}_{strm}$.

In order to fully mimic the experimental SCL images and include the streak of blue light emerging from the horn tip to the reactor bottom, two species were considered: *OH*$^\bullet$ radicals and an emitting species termed as photon equivalents (*PE*). This way, the interplay between the acoustic streaming and the light emission maps in the reactor can be resolved. Details on the equations and different reaction rates can be found in Section B.3. of the Supporting Information.

In the reaction system, the *OH*$^\bullet$ radicals are produced during cavitation collapse and are at the same time consumed by luminol, resulting in light emission. The amount of *OH*$^\bullet$ radicals produced during bubble collapse (*CP*) was calculated based on the regression formula derived by Hegedüs et al. [73,76], which is only valid for water. Therefore in this section only simulations for water were performed. By means of this regression formula (Eqs. (S13) to (S15) of the Supporting Information), *CP* was related to the local acoustic pressure and using Eq. (23), the overall rate of *OH*$^\bullet$ radicals generation in the reactor was determined. The Avogadro constant (N_a), frequency (f) and bubble volume fraction

(n_b) were used to obtain the correct dimensions. The acoustic pressure field was solved and was then used to calculate the rate of $OH^\bullet$ radicals generation.

$$R_{g,OH^\bullet} = \frac{CP}{N_a} \cdot n_b \cdot f \tag{23}$$

As luminol reacts with the sonochemically produced $OH^\bullet$ radicals, light is emitted. Therefore, the rate of *PE* production is directly related to the consumption of $OH^\bullet$ radicals. The consumption rate of $OH^\bullet$ radicals $R_c(OH^\bullet)$ was based on literature experiments, where a second-order reaction rate constant was found [21,96]. However, due to the excess of luminol during sonochemiluminescence experiments and to limit computational complexity, in this work the second order reaction kinetics were transformed to a pseudo first order reaction system in Eq. (24), with $c_{lum} = cte$, using the experimental data from our earlier work [23].

$$R_{c,OH^\bullet} = -8.7 \cdot 10^9 \cdot c_{OH^\bullet} \cdot c_{lum} \tag{24}$$

Moreover, reported SCL data indicates the light intensity does not disappear instantly, a more exponential decrease over time has been stated instead [100,101]. Therefore, a first order consumption reaction for the *PE* species was included. The distribution in the sonochemical reactor was visualized by plotting the *PE* concentration.

3.5. Meshing and boundary conditions

For all simulations, a two-dimensional axisymmetric geometry was applied. The numerical grid consisted of free triangular unstructured mesh elements and the number of mesh elements per wavelength satisfied the $k \cdot h << 1$ criterion, with h being the average size of the mesh elements and k the wavenumber [14,15,20,49]. In addition, corner and boundary layer refinements were performed.

To calculate the pressure field in the reactor, the sonotrode boundaries in contact with the liquid were coupled using the COMSOL acoustic-structure Multiphysics coupling. The sonotrode side walls that were not submersed in the liquid were assigned *free* boundaries, since the surrounding air does not exert a load on these sonotrode walls. At the top of the sonotrode a *prescribed displacement* was imposed. Due to lack of accurate measurements, the displacement magnitude (u_{in}) was swept to obtain agreements with both experimental calorimetry and SCL data [22] for each mixtures individually [30]. The liquid–air interface and reactor walls were all modelled *sound soft* in the *Pressure acoustics* module.

In the acoustic streaming calculations a stationary solver was used. The reactor and sonotrode walls were modelled with no-slip conditions. The liquid–air interface was modelled with full-slip conditions.

For all transport phenomena problems, transient simulations were computed. To predict the temperature gradients in the sonochemical reactor, a transient simulation of 180 s was performed, corresponding to the actual timing of the validation calorimetric experiments. All boundaries in contact with the outside air were assumed *adiabatic* (since the cooling jacket was emptied during the calorimetric experiments). To predict the full sonochemical light distribution in the reactor, a time-horizon of 15 s was simulated, which corresponds to a single SCL experiment. All boundary conditions were set to *no flux* since no species could leave the reactor.

4. Results and discussion

4.1. The effect of the medium viscosity on microscale

4.1.1. Cavitation threshold determination

Fig. 3 presents an overview of the different cavitation thresholds calculated for mixtures of increasing viscosity and a fixed bubble radius of $R_0 = 5$ μm.

Based on Fig. 3, some important observations are made. Firstly, the *Blake threshold* values are almost unaffected by the viscosity increase. Secondly, for the case of water, all pressure thresholds remained similar irrespectively of the approach implemented. Thirdly, an increasing trend of the threshold pressure with viscosity is visible for all threshold definitions except the Blake pressure. Additionally, for the highest viscosity solutions, large differences can be seen between the estimated thresholds. This indicates that viscosity plays an important role in the bubble collapse dynamics [71,102].

For mixtures of increasing viscosity, the Blake pressure is slightly lower compared to water due to the smaller surface tension of the PEG-water mixtures ($\sigma \sim 70$ mN/m for water compared to $\sigma \sim 55$ mN/m, respectively). Fig. 3 suggests that the *Blake threshold* is inadequate in predicting the acoustic pressure needed for a violent collapse in more viscous solutions. This can be explained by the major role of viscosity compared to the impact of surface tension, which cannot be predicted using the simple Blake formula [78]. It seems that the *ER threshold* is more moderate compared to the T_{max} and *Mach* criteria. For example, when solving the bubble dynamics for the more viscous solutions a pressure corresponding to the *ER threshold* generates collapse temperatures $\ll$1000 K, which is insufficient for the sonolysis of water [1,79,103]. Therefore, the *ER threshold* cannot be used to quantify a violent collapse and care should be taken when applying rule-of-thumb guidelines derived for water to more viscous solutions.

Two T_{max} *threshold* pressures were calculated, corresponding to a collapse temperature of 3000 K ($T_{max,3000K}$) and 5500 K ($T_{max,5500K}$). Both thresholds were larger than the *Blake* and *ER pressures*. Comparing the relative difference between the $T_{max,3000K}$ and $T_{max,5500K}$ thresholds, it can be seen that the $T_{max,3000K}$ threshold is less than 20 % lower (compare 1.5 bar to 1.2 bar for water), which comes in agreement with the work of Holland & Apfel [78]. Moreover, the *Mach* and $T_{max,5500K}$ thresholds are very similar and represent the largest required pressure values. For a sonic collapse, significant amount of energy is generated and transferred to the bubble content [71] which would result in extreme hot-spot temperatures. In view of comparison to SCL images which can be related to the bubble collapse temperature, in all following models the $T_{max,3000K}$ threshold is selected to indicate the occurrence of "efficient" cavitation. A maximum core temperature of 3000 K was chosen instead of 5500 K in order to avoid imposing collapse conditions that are too strict for SCL to occur.

4.1.2. Collapse-temperature

The relationship between the maximum bubble temperature over an

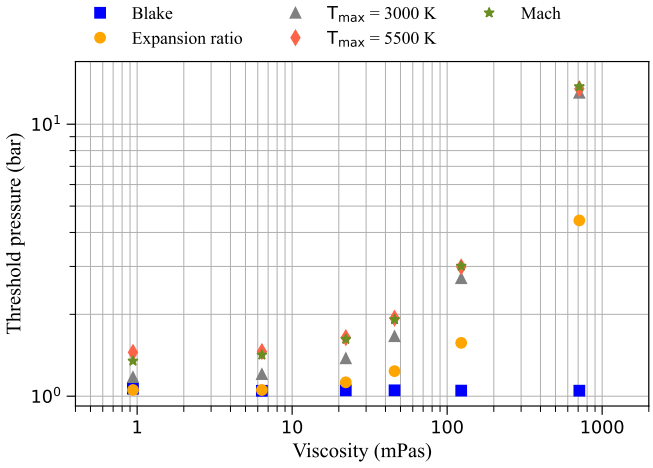

Fig. 3. Overview of the different cavitation threshold pressures calculated for mixtures of increasing viscosity for a single bubble with $R_0 = 5$ μm at a frequency of 30 kHz. For clarity, the threshold pressures are plotted on a logarithmic y-axis.

acoustic period and the non-dimensional driving pressure for the different viscosities was calculated and is shown in Fig. 4. When the driving pressure is below the cavitation threshold, the maximum is almost equal to the ambient temperature, since no violent cavitation collapse occurs. When the pressure is increased, the maximum temperature increases rapidly. Interestingly, when the driving pressure is increased further, the increase in collapse temperature becomes less pronounced as seen by the change in curvature of the curves. In the ideal non-dissipative case, as the driving pressure increases, the energy stored in the bubble during expansion increases which results in a higher hot-spot temperature during collapse. However, the energy dissipated by a single bubble also increases during bubble oscillations (see Fig. 5 in Section 4.1.3), which lowers the energy available to be transferred to the collapse. As a result, the combination of both competing effects results in a change in slope of the T_{max} curve.

The maximum temperature corresponding to the viscosity of 0.9 mPas (water) and 6.4 mPas (40 wt% PEG400), were found very similar $T_{max} = 11228$ K and $T_{max} = 11088$ K for $p/p_\infty = 5$, respectively (relative difference smaller than 5 %).

4.1.3. Energy dissipated by a single cavitation bubble

The viscous dissipation by a single oscillating bubble in function of the non-dimensional acoustic pressure is presented in Fig. 5. For all mixtures, the viscous losses were dominant over the thermal losses, which was even more distinct for the higher viscosity solutions. This corroborates earlier results reported for water [26] and supports the assumption of neglecting the thermal losses in Eq. (13), at least for the cases studied here.

At small driving pressures, the viscous dissipation is low, but above a certain value of the acoustic pressure the dissipation jumps due to the onset of violent non-linear oscillations of the cavitation bubbles [26]. For the largest viscosities (123.2 mPas and 712.5 mPas), the dissipated power shows a more gradual increase. Moreover, when the viscosity is increased to 712.5 mPas, for driving pressures of $p/p_\infty \geq 1$, small viscous dissipation is observed. Only at high driving pressures the viscous dissipation rises. This can be attributed to highly damped bubble oscillations at high viscosities [71,104]. Due to the large viscosity, both the bubble radius (R) and the bubble wall velocity ($\dot{R}$) amplitude during bubble oscillations become very small. As a result, in Eq. (3), even though the viscosity is larger the dissipated power is lower. Only at very high driving pressures the bubble motion becomes sufficiently violent to obtain large viscous dissipation.

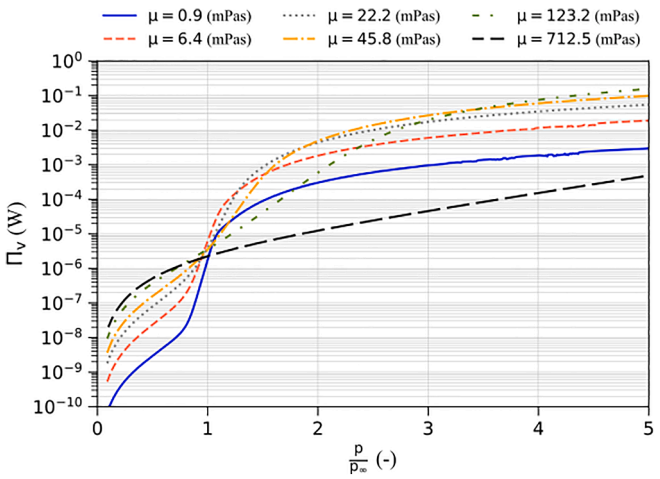

Fig. 5. Viscous power dissipation by a single cavitation bubble ($R_0 = 5$ μm) over one oscillation cycle at a frequency of 30 kHz. The driving pressure p is non-dimensionalized by the ambient pressure (p_∞).

4.2. The effect of the medium viscosity on macroscale

4.2.1. Comparison between sound attenuation models

A comparison was made for one specific value of the number of cavitation bubbles n_b. Fig. 6 presents the relative cavitation zone size predictions of each model for $n_b = 15$ 1/mm^3. A change in n_b would not affect the LE and TV models since they do not include cavitation-based attenuation.

A first observation can be made when comparing the LE (no attenuation) and TV (classical thermoviscous attenuation) models. Both models exhibit identical behavior in terms of cavitation zones predictions, which suggests that the classical thermoviscous attenuation is therefore probably negligible compared to the cavitation-based attenuation.

Counterintuitively, for $n_b = 15$ 1/mm^3 it seems the use of linear cavitation-based attenuation (CP model) results in larger amounts of cavitation in pure water compared to the LE and TV models. This can be explained by the linear dispersion effect of waves by cavitation bubbles. Indeed, in Eq. (10), the real part of the squared wavenumber k^2 depends on n_b [14], and since its imaginary part is comparatively small [85], the effective propagation wavelength $\lambda_{prop} = 2\pi/Re(k)$ is strongly dependent on n_b (for $n_b = 15$ 1/mm^3 the wavelength is $\lambda_{prop} = 4.49$ cm). To check

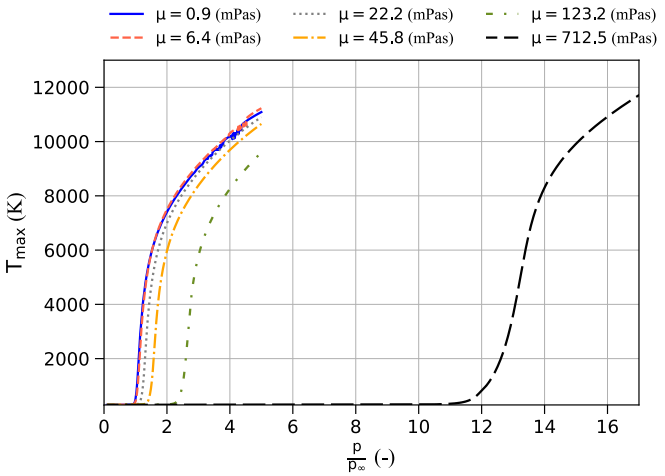

Fig. 4. Maximum temperature during one oscillation period for a single cavitation bubble of $R_0 = 5$ μm at a frequency of 30 kHz. The driving pressure p is non-dimensionalized by the ambient pressure (p_∞).

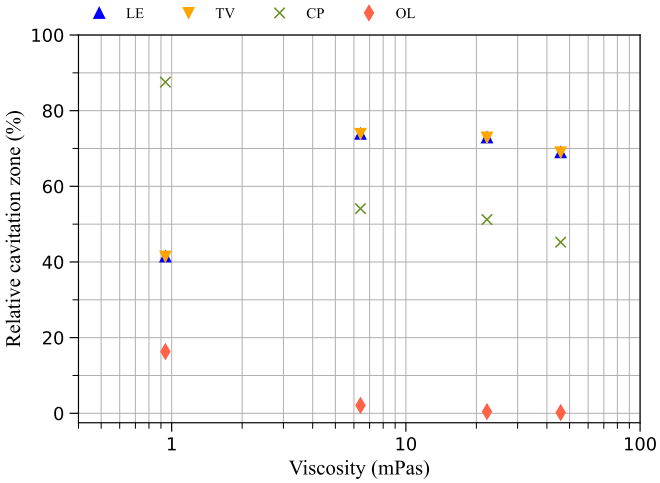

Fig. 6. Comparison of the sound attenuation models for $n_b = 15$ 1/mm^3. Key for the models: Linear elastic (LE), Classical Thermoviscous (TV), Commander-Prosperetti (CP) and Louisnard model (OL).

this effect, a COMSOL *Eigenfrequency study* was performed to determine the wavelength at which the liquid volume would become resonant. For the considered geometry this wavelength was found to $\lambda_{res} = 4.48$ cm, which is close to the effective propagation wavelength ($\lambda_{prop} = 4.49$ cm) at the driving frequency considered here. As a result, the CP model predicts that the liquid volume undergoes *numerical resonance*, resulting in large predicted acoustic pressures. We use here the term *numerical* to clarify that this resonance does not occur in real life, but is the result of the numerical model limitations. For a value of $n_b = 15$ 1/mm^3, λ_{prop} is equal to the resonance wavelength and larger cavitation zones are predicted for water. For the OL model no numerical resonance effects were observed, which is due to the larger attenuation contribution brought by the large values of $Im\left(k_{OL}^2\right)$ that blurs the resonance effect. This highlights the importance of using the real bubble dynamics to calculate energy dissipation instead of linearizing the bubble oscillations. For the CP model the more viscous solutions do not show numerical resonance, which might be partly attributed to the larger imaginary part of the wavenumber brought by the damping term b_{CP}, because of larger viscosity (Eq. (S12) in Table S4 of the Supporting Information).

4.2.2. Acoustic pressure field validation against SCL

The predictions of the acoustic pressure field based on the OL model are presented in Fig. 7 (top row). The cyan lines demarcate the zones where the acoustic pressure exceeds the cavitation threshold pressure and therefore indicate zones of increased likelihood of cavitation and SCL emissions. Results are shown for an ultrasonic frequency of 31 kHz, since for different frequencies the lateral cavitation zones around the horn shaft were not always predicted. This result indicates the nominal working frequency of a sonotrode should be carefully assessed when modelling the pressure fields.

Comparing the OL model with experimental SCL data (Fig. 7 bottom row), several agreements can be found. The model is able to predict the generation of multiple cavitation zones, seen experimentally: (1) right below the horn tip, and (2) around the horn shaft. However, for μ = 0.9 and μ = 6.4 mPas the model predicts the appearance of an additional cavitation zone below the sonotrode tip. At first, this zone does not seem visible in the SCL image, but as will be demonstrated in Section 4.4 the strong acoustic streaming jet can partly blur the light emissions that would occur by this additional cavitation zone below the horn tip. This would entail that using the SCL method not all active cavitation zones can be clearly visualized.

As mentioned before, the number of bubbles n_b and the input displacement were used as fitting parameters to obtain the best correspondence to SCL and calorimetry results. For the viscosities $\mu = 0.9$ to 45.8 mPas, the same number of bubbles of $n_b = 20$ 1/mm^3 was used. It is interesting to note that for an increase in viscosity, a larger input displacement u_{in} was required to obtain both the cavitation zone below the tip and the lateral cavitation zone covering the sonotrode shaft.

The model predicts a decreasing trend in the size of cavitation zones for an increase in viscosity. Experimentally, it seems that the viscosity $\mu = 6.4$ mPas (40 wt% PEG400) shows the brightest light emissions. However, when comparing the spatial extensions of light emission at $\mu = 6.4$ mPas with the one at $\mu = 0.9$ mPas (pure water), it seems that the light zone around the sonotrode shaft extends more slightly towards the reactor walls for pure water. The difference in light intensity might be due to the different properties and composition of the 40 wt% PEG400 mixture compared to water, such as the pH [105]. The presence of the PEG might influence the radical yields or experimental SCL light emissions. Moreover, the model assumes a monodisperse bubble distribution of $R_0 = 5$ μm for all viscosities, while in reality larger bubbles can be stable for larger viscosities [69]. Considering only the PEG-water mixtures, the model is able to capture a decrease of cavitation zone size with viscosity. It seems that as the viscosity increases, the spatial distribution of radicals decreases (shown by a decrease in extent of SCL light emissions).

4.2.3. Comparing thermoviscous and cavitation-based dissipation

The dissipated energy calculated with the CP and OL models was also compared to experimental calorimetric power measurements, shown in Fig. 8.

The shortcomings of the linear models (CP in this case) become clear as the predicted dissipated power is almost an order of magnitude too low for the same model conditions. This clearly highlights the inaccurate prediction of dissipation of the cavitation bubbles by the linear models. The OL model, on the contrary, predicts dissipated powers which are in the same order of magnitude and follow the same trend as the experimental values, shown in Fig. 8.

For the OL model, good correspondence between the predicted dissipated power and experimental calorimetric power can be remarked. For these points, n_b was fixed to 20 1/mm^3, only the input displacement u_{in} was used as a fitting parameter. When the viscosity increases (lower

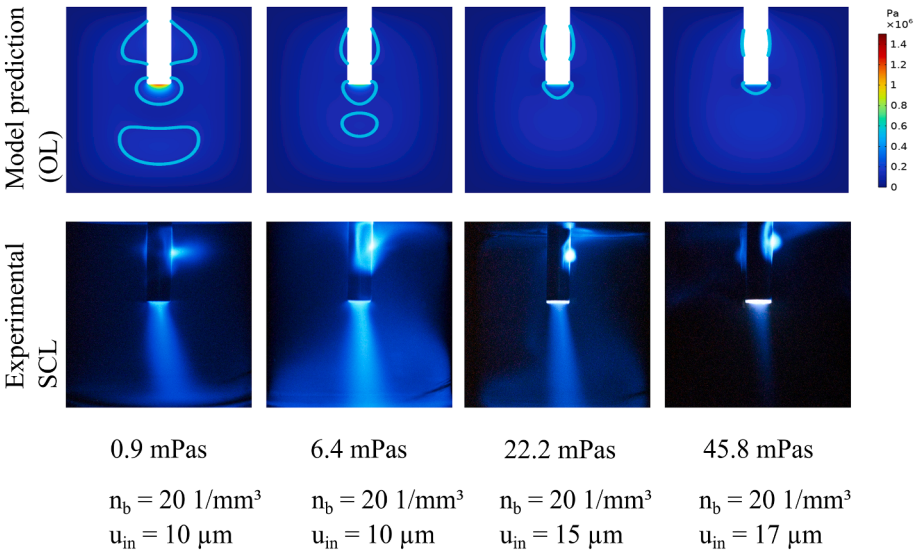

Fig. 7. Numerical model predictions (OL model, top row) compared to experimental SCL images (bottom row) for increasing viscosity solutions. In the model predictions, the color maps indicate the acoustic pressure field, while the cyan lines demarcate the zones of increased cavitation probability. The combinations for n_b and u_{in} used in the simulations are shown in the bottom row. The first column ($\mu = 0.9$ mPas) corresponds to pure water.

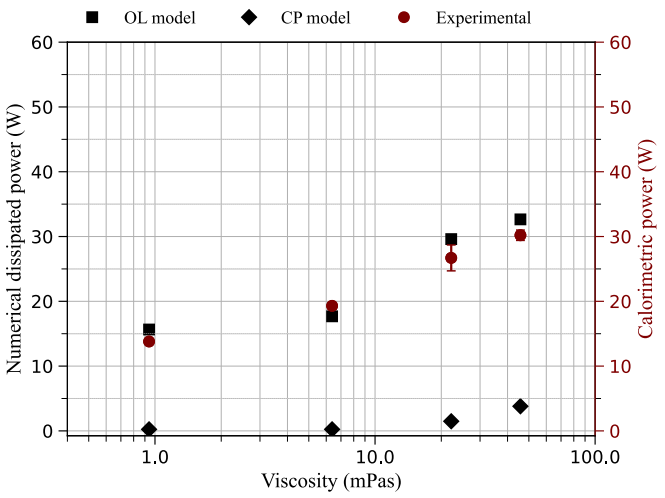

Fig. 8. Comparison of experimental calorimetry results with numerical predictions of dissipated power. Key for the legend: OL = Louisnard model, CP = Commander-Prosperetti model.

than $\mu = 123.2$ mPas), a larger u_{in} was required to match the experimental SCL image and calorimetric power.

Additionally, for the OL model, the energy balance was checked to verify the model accuracy. The energy flowing into the reactor across the lateral horn walls and tip was equal to the energy dissipated in the reactor bulk (relative difference $< 0.3\%$, possibly due to numerical errors).

Comparing the classical thermoviscous dissipation (based on the TV model) and cavitation-based dissipation (based on the OL model), it becomes apparent that cavitation dominates the dissipated power. The classical thermoviscous attenuation is only a fraction of the cavitation-based (factor 10^{-4}). From a more theoretical view it can also be expected that cavitation has a larger impact on the dissipated power due its smaller length scale, compared to the classical thermoviscous attenuation. A more detailed description can be found in Section C of the Supporting Information.

4.2.4. Acoustic streaming profile and bubble pathways

The acoustic streaming fields are presented in Fig. 9 (top row) for the mixtures of increasing viscosities. For all viscosities, a jet pointing towards the reactor bottom was predicted that seems to broaden and become more diffuse as viscosity is increased. Additionally, for water two contra-rotating vortices were predicted, while for the other viscosities only one main vortex was predicted. For water, Dahlem et al. [25] and more recently Rahimi et al. [106] were both able to visualize the formation of two contra-rotating vortices for a lower horn insertion depth. The primary vortex is created by the jet-like flow and its top part drags along the stagnant fluid on top of it, which creates the secondary vortex.

When the modelled streaming velocities of the acoustic jet are compared against available PIV experimental results [23] for the liquid jet, one main difference can be observed. The model seems to overpredict velocities. Right below the sonotrode, the highest discrepancy is remarked with differences up to a factor of 10 compared to the PIV experiments. However, in this localized zone the presence of cavitation itself interferes and introduces uncertainty in experimental velocity measurements. Alternatively, it seems that the Louisnard model predicted excessive gradients in the acoustic pressure near the transducer, possibly owed to the strong energy dissipation. As can be seen from Eqs. (16) to (18), the driving force for acoustic streaming does not explicitly depend on the acoustic pressure (P) but rather depends on the acoustic pressure gradient (∇P), which is correlated to the attenuation of the acoustic wave. Therefore, large local energy dissipation in the acoustic field may induce large driving forces in the acoustic streaming velocity. It should be noted that including additional damping terms in the Louisnard model (such as Π_{th} and Π_{rad}) may amplify the acoustic streaming velocity due to steeper pressure gradients below the sonotrode tip.

Additionally, the model predicts a decrease in jet velocity for an increase in viscosity. However, the PIV results indicated a lower streaming velocity for water compared to some viscous samples. This could possibly be attributed to the highly turbulent flow patterns which hindered an accurate velocity measurement by the PIV. This is supported by the general decreasing trend in measured velocity magnitude of the radial streamlines, which exhibit more ordered characteristics. Alternatively, similar to the SCL comparison, the addition of PEG might influence the bubble dynamics.

Using Eq. (19), the bubble pathways were calculated and are presented in Fig. 9 (bottom row). The streamlines represent the pathways that hypothetical bubbles generated at arbitrary spots within the reactor would follow. The "Launch sites" consist of zones where the acoustic pressure is 0.99 times the threshold pressure to visualize the bubble motion.

For all viscosities, the bubbles generated below the horn tip are

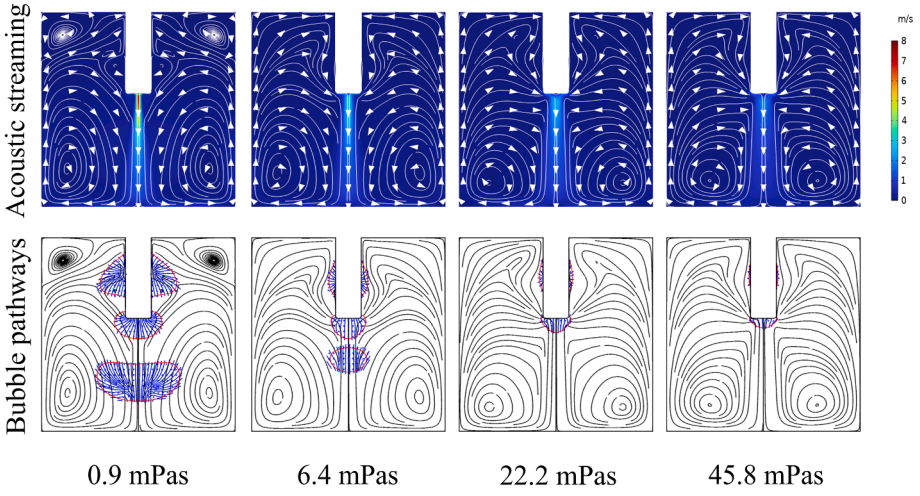

Fig. 9. OL model predictions for the Acoustic streaming profiles (white arrows, top row) and bubble pathways (blue arrows, bottom row). The bubble pathways are constructed by following the paths a bubble would follow if it was launched at an arbitrary spot in the reactor where the acoustic pressure is 99% of the threshold value. For reference to the bubble pathways, the cavitation threshold is drawn in red and the acoustic streaming profiles are drawn in black.

dispersed into the reactor bulk. This is in agreement with simulations and experimental observations of Lesnik et al. [31], although the latter work included much more complex population balances for the cavitation bubbles. It seems that both the generation of travelling waves at the horn tip and the acoustic streaming (black lines in Fig. 9 bottom row) invigorate each other and push the bubbles away from the horn tip. The bubble clusters at the horn wall seem to converge to a point close to the sonotrode lateral side, which seems to be confirmed by the point-like light emissions in the SCL images, especially for $\mu = 22.2$ and $\mu = 45.8$ mPas.

4.3. Coupling the acoustic calculations with heat transport

An overview of the spatial temperature profiles after 180 s of sonication can be found in Fig. 10. For water, no noticeable temperature differences can be remarked. When increasing the viscosity (starting from $\mu = 45.8$ mPas), small gradients start to occur with increased temperature zones located below the tip and along the horn axis.

The predicted temperature profiles were used as a tool to investigate the influence of location of the temperature probe during calorimetric measurements. Using, Eq. (25) the calorimetric power was calculated, taking the temperature slope over time $\frac{dT}{dt}$ at different locations in the reactor, m the mass of the solution in the reactor and c_p the specific heat capacity.

$$P_{cal} = mc_p\frac{dT}{dt} \tag{25}$$

The relative standard deviation of calorimetric power gradients in the reactor ranged from 0.10 % (for $\mu = 0.9$ mPas) to 0.14 % (for $\mu = 45.8$ mPas) when increasing the viscosity. As shown in Fig. S5 of the Supporting Information, larger temperature gradients start to occur for higher viscosities. However, for these points transducer pulsations occurred that could not be modelled, therefore results should be treated with caution. Nevertheless, considering the conservation of energy in an adiabatic system, despite the possible existence of large temperature gradients in the reactor, the calorimetric characterization should still give accurate information as long as multiple temperature probes are used to average its result as was done in reference [23].

The simulations indicate potential in the application of ultrasound in viscous systems. The acoustic streaming and cavitation oscillations might increase mixing in the reactor, so only relatively small temperature gradients might occur, even in viscous fluids. However, it should be noted that the convective energy transport is overestimated by the model, due to the overpredictions of the acoustic streaming jet velocity. Therefore, in reality heat generation as a result of the acoustic dissipation might still happen at a faster rate than the transport of heat in the reactor via acoustic streaming and conduction, which may modify ambient temperature conditions for bubbles in those zones, and influence their dynamics and sonochemical effects.

4.4. Coupling the acoustic calculations with reactions and mass transport

After solving the convection–diffusion equations, the light emission over time was computed by plotting the *PE* species concentration in the reactor. The left side of Fig. 11 shows the predicted light emission for sonication of 15 s, the right side shows an experimental SCL image for the same conditions. Only a gradient coloring is presented, since the exact values for the *PE* concentrations do not present any physical meaning.

The updated model predicts a lateral cavitation zone covering the horn shaft which was also confirmed experimentally by the Aluminum foil erosion technique [23]. The shape of predicted light emission looks similar to the pure acoustic fields calculations in Fig. 7. However, in the SCL image, the light emission seems to move more horizontally compared to the model predictions. As shown by Vargas et al. [107], the curvature of the reactor can cause distortion of the images by refraction effects. More specifically, lateral cavitation zones appeared to be larger and more off-axis than in the corrected images. Therefore, a direct comparison of the shape of light emission of model predictions to the experimental SCL visualization can be speculative for these lateral light zones.

The cavitation zone directly under the tip was reasonably predicted.

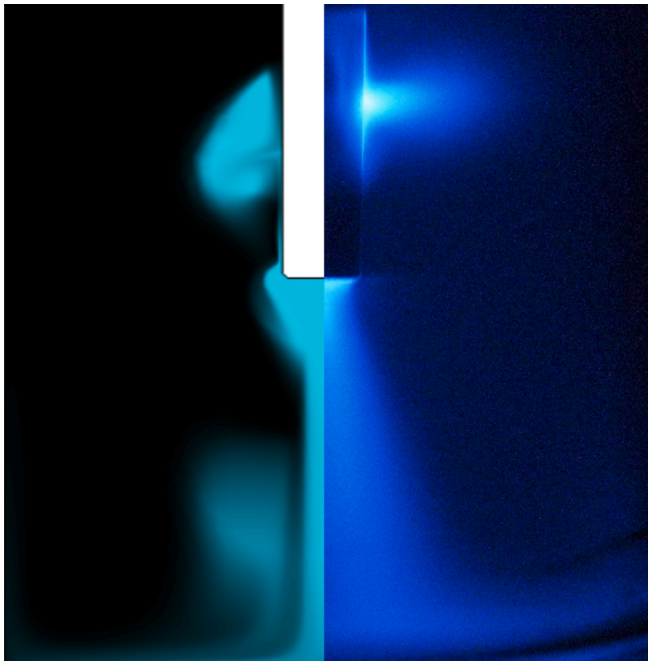

Fig. 11. Comparison of the Photon Equivalent species (PE) concentration (left) against experimental SCL light emissions (right) for sonication of water ($\mu = 0.9$ mPas), computed for $n_b = 20$ 1/mm^3 and $u_{in} = 10$ μm.

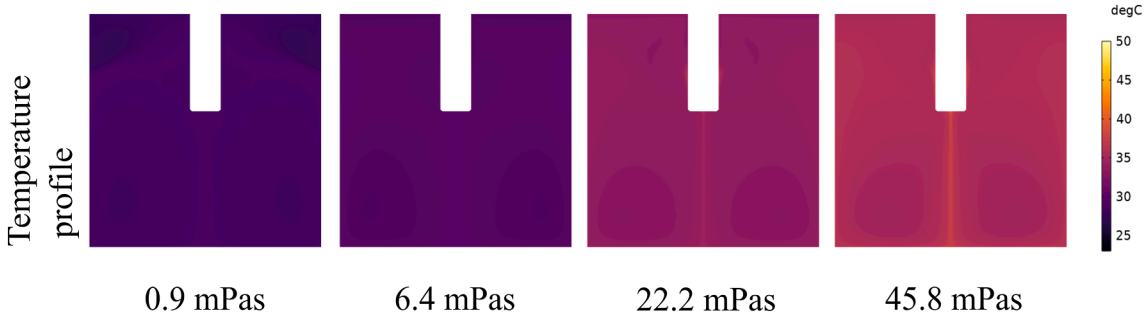

Fig. 10. Predicted spatial temperature profiles after 180 s of sonication for increasing viscosity solutions. Temperatures are displayed in degrees Celsius.

In particular, it can be seen that the bright streak of light emerging from the reactor tip and splashing on the bottom of the reactor, visible on the luminol map (Fig. 11 right part), is reproduced by the *PE* concentration computation (Fig. 11 left part). However, it does seem that the predicted jet is thinner compared to experimental image. It is interesting to note that this jet-like structure does not appear on the acoustic pressure map of Fig. 7.

Moreover, the light emissions of the additional cavitation zone below the sonotrode tip are partly blurred by the acoustic streaming motion. The *PE* concentration, which corresponds to light emission, is half of the *PE* concentration directly underneath the sonotrode tip. Due to the time delay in the light emission, the light produced in the additional cavitation zone under the tip is transported into the bulk by the streaming motion. This results in a smearing out of the light, which makes it difficult to identify the active zone of acoustic cavitation and which might create the perception of a broader jet flow.

The bubble pathways calculations (see Fig. 9) revealed that cavitation bubbles are nucleated at the tip, and are simultaneously transported within the reactor to create distant bubble clouds. Moreover, the calculation of the acoustic pressure field at the reactor bottom indicates that the maximum temperature of a bubble hypothetically collapsing at the bottom of the reactor is too low to generate SCL emissions. This is consistent with observations of Yusuf et al. [108], which were not able to experimentally measure shockwaves for such distant bubble clusters and concluded that these bubbles could not cavitate inertially. This suggests that the streak of faint light emission under the sonotrode should be attributed to the motion of excited luminol species exhibiting light emission delay time.

The above results shed new light on the interpretation of SCL images. Our simulations indicate that a high luminol intensity in some reactor zones might not always correspond to a high sonochemical activity in that region or that active zones can be blurred by acoustic streaming during the SCL method since the dispersion of light emission may be mediated by acoustic streaming transporting species whose de-excitation is sufficiently slow. This suggests that SCL light generation should be partially decoupled from active cavitation. If this conjecture was true, this would mean that in a fully experimental campaign, the SCL technique could better be combined with different cavitation mapping measurements, such as aluminum foil erosion, high speed imaging of bubble clusters or chemical dosimetry for overall reactor performance qualification.

To the authors' best knowledge, the current model approach is the first one to predict experimental SCL images. However, it should be mentioned that the current model is underpinned by several assumptions, for example the luminol emission delay time is used as a fitting factor. Nevertheless, we expect the inclusion of transport equations and chemical reactions in sonochemical models to offer new avenues in validating sonochemical reactor models. In this framework, the work of the *Hegedüs* group seems of prime importance in providing ready-to-use analytical expressions of radical yields in function of the bubble expansion ratio [73,76].

5. Conclusions and outlook

The current work extended the non-linear *Louisnard* model for modelling ultrasound fields and provided new strategies in modelling sonochemical reactors by coupling acoustic calculations with heat and mass balances. Firstly, to expand the operation range of the acoustic model, acoustic field calculations were applied to viscous fluids. The effect of viscosity on acoustic attenuation was emphasized and classical thermoviscous and cavitation-based attenuation mechanisms were directly compared. Both the micro-and macroscales were resolved by solving the bubble dynamics equations of a single bubble and by predicting the acoustic pressure and velocity fields, respectively. Secondly, heat transport effects in a sonochemical reactor were modelled, by coupling the acoustic calculations with an energy balance. Thirdly, reactions and mass transport were modelled in a sonochemical reactor, by considering the SCL reaction in a sonicated water-luminol system. The model results were compared to available experimental results in terms of cavitation generation (experimental SCL images), energy dissipation (calorimetry measurements) and streaming profiles (PIV experiments) [23].

On the microscale, the effect of the viscosity on the threshold pressure for cavitation to occur was determined. In this regard several definitions for the cavitation threshold were selected and calculated for the viscous mixtures. The applicability of the *Blake* and *Expansion Ratio* thresholds to more viscous solutions was found inaccurate, and therefore it was suggested to define a threshold pressure based on the collapse temperature of a single bubble. The viscous energy dissipated by a single bubble was quantified and it was shown that an increase in viscosity does not necessarily indicate an increase in viscous dissipation. At high viscosities the bubble oscillations become overdamped which lowers the dissipation rate.

On the macroscale, the limitation of linear cavitation-based models became apparent by the generation of numerical resonance due to an improper prediction of the wavelength dispersion and underprediction of energy dissipation. The non-linear *Louisnard* model did not suffer from this drawback and was validated against SCL for the prediction of cavitation zones, and calorimetry for the dissipation of energy. The simulations were able to predict correctly the generation of two cavitation zones (at the horn tip and around the horn shaft). However, the model predicted the appearance of a third cavitation zone for $\mu = 0.9$ and $\mu = 6.4$ mPas that at first does not seem visible in the SCL image. The energy calculations showed that the thermoviscous attenuation is negligible compared to the cavitation-based attenuation by several orders of magnitude even for the highest viscosity. Additionally, using the acoustic pressure field predictions, the acoustic streaming profiles and bubble pathways were calculated.

Heat transport equations were incorporated in the acoustic fields calculations. As a result, the temperature field inside a sonochemical reactor was predicted for mixtures of increasing viscosity and it was shown that small gradients can appear with an increase in viscosity, which propagates to small gradients in calorimetric power depending on the spatial location of the temperature probe during the measurement.

Lastly, chemical reactions and mass transport were coupled with the acoustic field calculations to model the SCL reaction of sonicated luminol solutions and coherent light emissions in a sonochemical reactor. First simulations indicate the streak of faint blue light emission under the horn tip can be the result of excited luminol species being dragged by either the acoustic streaming or the moving cavitation bubbles. Moreover, light emissions of active cavitation zones can be blurred by the acoustic streaming motion. Therefore, care should be taken in the interpretation of SCL glowing zones, which do not necessarily directly correspond to inertial cavitation zones.

Future work could first include the improvement of the shortcomings of the non-linear acoustic modelling approach. Particularly, the current model assumes a monodisperse cavitation distribution of bubbles of the same size independently of viscosity. However, GPU simulations by the *Hegedüs* group indicate that a higher viscosity increases the maximum stable bubble size [69]. It might be interesting to combine the bubble size calculations with the model proposed in this manuscript. Moreover, another improvement of the acoustic model could be made by using the extensions to Louisnard model developed independently by Trujillo [64], and Sojahrood et al. [66,67]. Whereas the Louisnard model assumes a linear dispersion relation for the real part of the squared wavenumber $Re\left(k_m^2\right)$, in Trujillo or Sojarhood models, the latter is derived rigorously from Caflisch equations, assuming mono-harmonic oscillations. This may alter both the sound speed and the attenuation in bubbly zones, and recent measurements in water seeded with contrast agents exhibit remarkable agreement between the computed and experimental values [82]. Then, the discrepancy between computed

acoustic streaming velocities and PIV experiments remains unclear and should be further investigated. More importantly, the extension of the novel SCL validation procedure to more viscous cases is aimed at, which would require extension of the semi-empirical equations of the *Hegedüs* group.

CRediT authorship contribution statement

Quinten Goris: Writing – review & editing, Writing – original draft, Visualization, Validation, Software, Methodology, Investigation, Data curation, Conceptualization. **Ariana Bampouli:** Writing – review & editing, Investigation, Data curation. **Mohammed Noorul Hussain:** Writing – review & editing, Investigation, Data curation. **Olivier Louisnard:** Writing – review & editing, Software, Investigation, Data curation. **Georgios D. Stefanidis:** Writing – review & editing, Supervision, Methodology, Funding acquisition. **Tom Van Gerven:** Writing – review & editing, Supervision, Resources, Project administration, Methodology, Funding acquisition, Conceptualization.

Declaration of competing interest

The authors declare that they have no known competing financial interests or personal relationships that could have appeared to influence the work reported in this paper.

Acknowledgments

Funding by the European Union's Horizon research and innovation programmes is gratefully acknowledged by Quinten Goris for the SIMPLI-DEMO project (grant agreement No 101058279) and Ariana Bampouli for the SIMPLIFY project (grant agreement No 820716). Additionally, the ESS travel grant provided the opportunity for Quinten Goris to perform a fruitful visit to the IMT Mines-Albi institute.

Appendix A. Supplementary data

Supplementary data to this article can be found online at https://doi.org/10.1016/j.ultsonch.2024.107114.

References

[1] K.S. Suslick, G.J. Price, Applications of ultrasound to materials chemistry, Annu. Rev. Mater. Sci. 29 (1) (Aug. 1999) 295–326, https://doi.org/10.1146/annurev.matsci.29.1.295.
[2] G.J. Price, E.J. Lenz, C.W.G. Ansell, The effect of high intensity ultrasound on the synthesis of some polyurethanes, Eur. Polym. J. 38 (8) (2002) 1531–1536, https://doi.org/10.1016/S0014-3057(02)00039-3.
[3] T. G. McKenzie, F. Karimi, M. Ashokkumar, and G. G. Qiao, "Ultrasound and Sonochemistry for Radical Polymerization: Sound Synthesis," Apr. 11, 2019, Wiley-VCH Verlag. doi: 10.1002/chem.201803771.
[4] S. Kentish, H. Feng, Applications of power ultrasound in food processing, Annu. Rev. Food Sci. Technol. 5 (1) (2014) 263–284, https://doi.org/10.1146/annurev-food-030212-182537.
[5] V.S. Sutkar, P.R. Gogate, Design aspects of sonochemical reactors: techniques for understanding cavitational activity distribution and effect of operating parameters, Dec. 01, 2009. doi: 10.1016/j.cej.2009.07.021.
[6] D. Meroni, R. Djellabi, M. Ashokkumar, C. L. Bianchi, D.C. Boffito, Sonoprocessing: From Concepts to Large-Scale Reactors, Feb. 09, 2022, American Chemical Society. doi: 10.1021/acs.chemrev.1c00438.
[7] M. Ashokkumar, "The characterization of acoustic cavitation bubbles - An overview", in *Ultrasonics Sonochemistry*, Elsevier b.v. (2011) 864–872, https://doi.org/10.1016/j.ultsonch.2010.11.016.
[8] S.J. Lighthill, Acoustic streaming, J. Sound Vib. 61 (3) (1978) 391–418, https://doi.org/10.1016/0022-460X(78)90388-7.
[9] S. Boluriaan, P.J. Morris, Acoustic streaming: from Rayleigh to today, Int. J. Aeroacoust. 2 (3) (Jul. 2003) 255–292, https://doi.org/10.1260/147547203322986142.
[10] J. Jordens, B. Bamps, B. Gielen, L. Braeken, T. Van Gerven, The effects of ultrasound on micromixing, Ultrason. Sonochem. 32 (Sep. 2016) 68–78, https://doi.org/10.1016/j.ultsonch.2016.02.020.
[11] H. Monnier, A.-M. Wilhelm, H. Delmas, Influence of ultrasound on mixing on the molecular scale for water and viscous liquids, Ultrason. Sonochem. 6 (1) (1999) 67–74, https://doi.org/10.1016/S1350-4177(98)00034-0.
[12] H. Monnier, A.M. Wilhelm, H. Delmas, The influence of ultrasound on micromixing in a semi-batch reactor, Chem. Eng. Sci. 54 (13) (1999) 2953–2961, https://doi.org/10.1016/S0009-2509(98)00335-2.
[13] Y.C. Wang, M.C. Yao, Realization of cavitation fields based on the acoustic resonance modes in an immersion-type sonochemical reactor, Ultrason. Sonochem. 20 (1) (2013) 565–570, https://doi.org/10.1016/j.ultsonch.2012.07.026.
[14] R. Jamshidi, B. Pohl, U.A. Peuker, G. Brenner, Numerical investigation of sonochemical reactors considering the effect of inhomogeneous bubble clouds on ultrasonic wave propagation, Chem. Eng. J. 189–190 (May 2012) 364–375, https://doi.org/10.1016/j.cej.2012.02.029.
[15] V. Sáez, A. Frías-Ferrer, J. Iniesta, J. González-García, A. Aldaz, E. Riera, "Chacterization of a 20 kHz sonoreactor. Part I: Analysis of mechanical effects by classical and numerical methods", in *Ultrasonics Sonochemistry*, Elsevier b.v. (2005) 59–65, https://doi.org/10.1016/j.ultsonch.2004.06.011.
[16] R. Christensen, P. Juhl, and V. Cutanda Henriquez, "Practical modeling of acoustic losses in air due to heat conduction and viscosity," in Proceedings - European Conference on Noise Control, 2008, pp. 3269–3274. doi: 10.1121/1.2934165.
[17] O. Assia, D. Hakim, "Propagation of Ultrasonic Waves in Viscous Fluids", in Wave Propagation in Materials for Modern Applications, INTECH (2010), https://doi.org/10.5772/6857.
[18] S. L. Garrett, Understanding Acoustics: An Experimentalist's View of Sound and Vibration Second Edition. doi: https://doi.org/10.1007/978-3-030-44787-8.
[19] P.M. Morse, K. Ingard Uno, Theoretical Acoustics. Mcgraw-Hill (1987).
[20] J. Klíma, A. Frias-Ferrer, J. González-García, J. Ludvík, V. Sáez, J. Iniesta, Optimisation of 20 kHz sonoreactor geometry on the basis of numerical simulation of local ultrasonic intensity and qualitative comparison with experimental results, Ultrason. Sonochem. 14 (1) (2007) 19–28, https://doi.org/10.1016/j.ultsonch.2006.01.001.
[21] H.N. McMurray, B.P. Wilson, Mechanistic and spatial study of ultrasonically induced luminol chemiluminescence, Chem. A Eur. J. 103 (20) (May 1999) 3955–3962, https://doi.org/10.1021/jp984503r.
[22] I. Garcia-Vargas, L. Barthe, P. Tierce, O. Louisnard, Simulations of a full sonoreactor accounting for cavitation, Ultrason. Sonochem. 91 (Dec. 2022), https://doi.org/10.1016/j.ultsonch.2022.106226.
[23] A. Bampouli, Q. Goris, J. Van Olmen, S. Solmaz, M. Noorul Hussain, G. D. Stefanidis, T. Van Gerven, Understanding the ultrasound field of high viscosity mixtures: Experimental and numerical investigation of a lab scale batch reactor, Ultrason. Sonochem. 97 (Jul. 2023), https://doi.org/10.1016/j.ultsonch.2023.106444.
[24] D. Fuster, A Review of Models for Bubble Clusters in Cavitating Flows, Mar. 01, 2019, Springer Netherlands. doi: 10.1007/s10494-018-9993-4.
[25] O. Dahlem, J. Reisse, V. Halloin, The radially vibrating horn: a scaling-up possibility for sonochemical reactions, Chem. Eng. Sci. 54 (13) (1999) 2829–2838, https://doi.org/10.1016/S0009-2509(98)00356-X.
[26] O. Louisnard, A simple model of ultrasound propagation in a cavitating liquid. Part I: Theory, nonlinear attenuation and traveling wave generation, Ultrason. Sonochem. 19 (1) (2012) 66–76, https://doi.org/10.1016/j.ultsonch.2011.06.008.
[27] S. Labouret, J. Frohly, Bubble size distribution estimation via void rate dissipation in gas saturated liquid. Application to ultrasonic cavitation bubble fields, EPJ Appl. Phys. 19 (1) (2002) 39–54, https://doi.org/10.1051/epjap:2002047.
[28] M. T. Tejedor Sastre, C. Vanhille, "A numerical model for the study of the difference frequency generated from nonlinear mixing of standing ultrasonic waves in bubbly liquids," Ultrason Sonochem, vol. 34, pp. 881–888, Jan. 2017, doi: 10.1016/j.ultsonch.2016.07.020.
[29] C. Vanhille, C. Campos-Pozuelo, Nonlinear ultrasonic propagation in bubbly liquids: a numerical model, Ultrasound Med. Biol. 34 (5) (May 2008) 792–808, https://doi.org/10.1016/j.ultrasmedbio.2007.11.004.
[30] O. Louisnard, A viable method to predict acoustic streaming in presence of cavitation, Ultrason Sonochem 35 (Mar. 2017) 518–524, https://doi.org/10.1016/j.ultsonch.2016.09.013.
[31] S. Lesnik, A. Aghelmaleki, R. Mettin, G. Brenner, Modeling acoustic cavitation with inhomogeneous polydisperse bubble population on a large scale, Ultrason. Sonochem. 89 (Sep. 2022), https://doi.org/10.1016/j.ultsonch.2022.106060.
[32] R. Mettin, I. Akhatov, U. Parlitz, C.D. Ohl, W. Lauterborn, Bjerknes forces between small cavitation bubbles in a strong acoustic field, Phys. Rev. E 56 (3) (Sep. 1997) 2924–2931, https://doi.org/10.1103/PhysRevE.56.2924.
[33] E. Riedel, M. Liepe, and S. Scharf, "Simulation of ultrasonic induced cavitation and acoustic streaming in liquid and solidifying aluminum," Metals (Basel), vol. 10, no. 4, Apr. 2020, doi: 10.3390/met10040476.
[34] F.J. Trujillo, A strict formulation of a nonlinear Helmholtz equation for the propagation of sound in bubbly liquids. Part I: Theory and validation at low acoustic pressure amplitudes, Ultrason. Sonochem. 47 (Oct. 2018) 75–98, https://doi.org/10.1016/j.ultsonch.2018.04.014.
[35] I. Tudela, V. Sáez, M. D. Esclapez, M. I. Díez-García, P. Bonete, and J. González-García, "Simulation of the spatial distribution of the acoustic pressure in sonochemical reactors with numerical methods: A review," 2014, Elsevier B.V. doi: 10.1016/j.ultsonch.2013.11.012.
[36] K.W. Commander, A. Prosperetti, Linear pressure waves in bubbly liquids: comparison between theory and experiments, J. Acoust. Soc. Am. 85 (2) (Feb. 1989) 732–746, https://doi.org/10.1121/1.397599.
[37] L. Van Wijngaarden, On the equations of motion for mixtures of liquid and gas bubbles, J. Fluid Mech. 33 (3) (1968) 465–474, https://doi.org/10.1017/S002211206800145X.

[38] L.V. Wijngaarden, One-dimensional flow of liquids containing small gas bubbles, Annu. Rev. Fluid Mech. 4 (1) (Jan. 1972) 369–396, https://doi.org/10.1146/annurev.fl.04.010172.002101.
[39] R.E. Caflisch, M.J. Miksis, G.C. Papanicolaou, L. Ting, Effective equations for wave propagation in bubbly liquids, J. Fluid Mech. 153 (1985) 259–273, https://doi.org/10.1017/S0022112085001252.
[40] J.K. Chu, T.J. Tiong, S. Chong, U.A. Asli, Y.H. Yap, Multi-frequency sonoreactor characterisation in the frequency domain using a semi-empirical bubbly liquid model, Ultrason. Sonochem. 80 (Dec. 2021), https://doi.org/10.1016/j.ultsonch.2021.105818.
[41] S.S. Rashwan, A. Mohany, I. Dincer, Development of efficient sonoreactor geometries for hydrogen production, Int. J. Hydrogen Energy 46 (29) (Apr. 2021) 15219–15240, https://doi.org/10.1016/j.ijhydene.2021.02.113.
[42] Z. Wei, L.K. Weavers, Combining COMSOL modeling with acoustic pressure maps to design sono-reactors, Ultrason. Sonochem. 31 (Jul. 2016) 490–498, https://doi.org/10.1016/j.ultsonch.2016.01.036.
[43] S. Fukunaga, et al., Effect of geometrical configuration of reactor on a ZrP nano-dispersion process using ultrasonic irradiation, Ultrason Sonochem 52 (Apr. 2019) 157–163, https://doi.org/10.1016/j.ultsonch.2018.11.008.
[44] V.S. Sutkar, P.R. Gogate, L. Csoka, Theoretical prediction of cavitational activity distribution in sonochemical reactors, Chem. Eng. J. 158 (2) (Apr. 2010) 290–295, https://doi.org/10.1016/j.cej.2010.01.049.
[45] L. Csoka, S.N. Katekhaye, P.R. Gogate, Comparison of cavitational activity in different configurations of sonochemical reactors using model reaction supported with theoretical simulations, Chem. Eng. J. 178 (Dec. 2011) 384–390, https://doi.org/10.1016/j.cej.2011.10.037.
[46] Q. Tang, J. Hu, Diversity of acoustic streaming in a rectangular acoustofluidic field, Ultrasonics 58 (Apr. 2015) 27–34, https://doi.org/10.1016/j.ultras.2014.11.015.
[47] J.K. Chu, T.J. Tiong, S. Chong, U.A. Asli, Investigation on different time-harmonic models using FEM for the prediction of acoustic pressure fields in a pilot-scale sonoreactor, Chem. Eng. Sci. 247 (Jan. 2021), https://doi.org/10.1016/j.ces.2021.116912.
[48] R. Jamshidi, D. Rossi, N. Saffari, A. Gavriilidis, L. Mazzei, Investigation of the effect of ultrasound parameters on continuous sonocrystallization in a millifluidic device, Cryst. Growth Des. 16 (8) (Aug. 2016) 4607–4619, https://doi.org/10.1021/acs.cgd.6b00696.
[49] D. Rossi, R. Jamshidi, N. Saffari, S. Kuhn, A. Gavriilidis, L. Mazzei, Continuous-flow sonocrystallization in droplet-based microfluidics, Cryst. Growth Des. 15 (11) (Nov. 2015) 5519–5529, https://doi.org/10.1021/acs.cgd.5b01153.
[50] H. Peng, P. Lu, P. Zhu, B. Yu, Acoustic calculation in low frequency sonopheresis based on bubble dynamics, J. Vibroeng. 19 (1) (2017) 592–603, https://doi.org/10.21595/jve.2016.17054.
[51] Y. Fang, T. Yamamoto, S. Komarov, Cavitation and acoustic streaming generated by different sonotrode tips, Ultrason. Sonochem. 48 (Nov. 2018) 79–87, https://doi.org/10.1016/j.ultsonch.2018.05.011.
[52] K. Fattahi, E. Robert, D.C. Boffito, Numerical and experimental investigation of the cavitation field in horn-type sonochemical reactors, Chem. Eng. Process. - Process Intesif. 182 (Dec. 2022), https://doi.org/10.1016/j.cep.2022.109186.
[53] M.N. Hussain, I. Janajreh, Acousto-chemical analysis in multi-transducer sonochemical reactors for biodiesel production, Ultrason. Sonochem. 40 (Jan. 2018) 184–193, https://doi.org/10.1016/j.ultsonch.2017.07.009.
[54] T. Yamamoto, S.V. Komarov, Influence of ultrasound irradiation on transient solidification characteristics in DC casting process: Numerical simulation and experimental verification, J. Mater. Process. Technol. 294 (Aug. 2021), https://doi.org/10.1016/j.jmatprotec.2021.117116.
[55] C. Yamaya and H. Inoue, "Behavior of propagation and heating due to absorption of ultrasound in medium," Japanese Journal of Applied Physics, Part 1: Regular Papers and Short Notes and Review Papers, vol. 45, no. 5 B, pp. 4429–4434, May 2006, doi: 10.1143/JJAP.45.4429.
[56] G.V. Norton, R.D. Purrington, The Westervelt equation with viscous attenuation versus a causal propagation operator: A numerical comparison, J. Sound Vib. 327 (1–2) (Oct. 2009) 163–172, https://doi.org/10.1016/j.jsv.2009.05.031.
[57] M. Solovchuk, T.W.H. Sheu, M. Thiriet, Simulation of nonlinear Westervelt equation for the investigation of acoustic streaming and nonlinear propagation effects, J. Acoust. Soc. Am. 134 (5) (Nov. 2013) 3931–3942, https://doi.org/10.1121/1.4821201.
[58] R. Velasco-Segura, P.L. Rendón, A finite volume approach for the simulation of nonlinear dissipative acoustic wave propagation, Wave Motion 58 (Nov. 2015) 180–195, https://doi.org/10.1016/j.wavemoti.2015.05.006.
[59] C. Delacour, D.S. Stephens, C. Lutz, R. Mettin, S. Kuhn, Design and characterization of a scaled-up ultrasonic flow reactor, Org. Process Res. Dev. 24 (10) (Oct. 2020) 2085–2093, https://doi.org/10.1021/acs.oprd.0c00148.
[60] G.S.B. Lebon, I. Tzanakis, K. Pericleous, D. Eskin, P.S. Grant, Ultrasonic liquid metal processing: The essential role of cavitation bubbles in controlling acoustic streaming, Ultrason. Sonochem. 55 (Jul. 2019) 243–255, https://doi.org/10.1016/j.ultsonch.2019.01.021.
[61] O. Louisnard, A simple model of ultrasound propagation in a cavitating liquid. Part II: Primary Bjerknes force and bubble structures, Ultrason Sonochem 19 (1) (2012) 56–65, https://doi.org/10.1016/j.ultsonch.2011.06.007.
[62] B.E. Sarac, D.S. Stephens, J. Eisener, J.M. Rosselló, R. Mettin, Cavitation bubble dynamics and sonochemiluminescence activity inside sonicated submerged flow tubes, Chem. Eng. Process. - Process Intesif. 150 (Apr. 2020), https://doi.org/10.1016/j.cep.2020.107872.
[63] G.S.B. Lebon, G. Salloum-Abou-Jaoude, D. Eskin, I. Tzanakis, K. Pericleous, P. Jarry, Numerical modelling of acoustic streaming during the ultrasonic melt treatment of direct-chill (DC) casting, Ultrason. Sonochem. 54 (Jun. 2019) 171–182, https://doi.org/10.1016/j.ultsonch.2019.02.002.
[64] F.J. Trujillo, A strict formulation of a nonlinear Helmholtz equation for the propagation of sound in bubbly liquids. Part II: Application to ultrasonic cavitation, Ultrason. Sonochem. 65 (Jul. 2020), https://doi.org/10.1016/j.ultsonch.2020.105056.
[65] C. Beckwith, G. Djambazov, K. Pericleous, C. Tonry, Comparison of frequency domain and time domain methods for the numerical simulation of contactless ultrasonic cavitation, Ultrason. Sonochem. 89 (Sep. 2022), https://doi.org/10.1016/j.ultsonch.2022.106138.
[66] A.J. Sojahrood, Q. Li, H. Haghi, T.M. Porter, M.C. Kolios, Investigation of the nonlinear propagation of ultrasound through a bubbly medium including multiple scattering and bubbl-bubble interaction: Theory and experiment, in: 2017 IEEE International Ultrasonics Symposium (IUS), 2017, p. 1, https://doi.org/10.1109/ULTSYM.2017.8092876.
[67] A.J. Sojahrood, H. Haghi, R. Karshafian, M.C. Kolios, Nonlinear model of acoustical attenuation and speed of sound in a bubbly medium, IEEE International Ultrasonics Symposium (IUS) 2015 (2015) 1–4, https://doi.org/10.1109/ULTSYM.2015.0086.
[68] F. Burdin, N.A. Tsochatzidis, P. Guiraud, A.M. Wilhelm, H. Delmas, Characterisation of the acoustic cavitation cloud by two laser techniques, Ultrason. Sonochem. 6 (1) (1999) 43–51, https://doi.org/10.1016/S1350-4177(98)00035-2.
[69] K. Klapcsik, F. Hegedűs, Study of non-spherical bubble oscillations under acoustic irradiation in viscous liquid, Ultrason. Sonochem. 54 (Jun. 2019) 256–273, https://doi.org/10.1016/j.ultsonch.2019.01.031.
[70] S. Hilgenfeldt, D. Lohse, M.P. Brenner, Phase diagrams for sonoluminescing bubbles, Phys. Fluids 8 (11) (1996) 2808–2826, https://doi.org/10.1063/1.869131.
[71] S. Hilgenfeldt, M. P. Brenner, S. Grossmann, and D. Lohse, "Analysis of Rayleigh-Plesset dynamics for sonoluminescing bubbles," May 1998, doi: 10.1017/S0022112098001207.
[72] R. Toegel, B. Gompf, R. Pecha, D. Lohse, Does Water Vapor Prevent Upscaling Sonoluminescence? Phys. Rev. Lett. 85 (15) (Oct. 2000) 3165–3168, https://doi.org/10.1103/PhysRevLett.85.3165.
[73] C. Kalmár, K. Klapcsik, F. Hegedűs, Relationship between the radial dynamics and the chemical production of a harmonically driven spherical bubble, Ultrason. Sonochem. 64 (Jun. 2020), https://doi.org/10.1016/j.ultsonch.2020.104989.
[74] K. Yasui, Production of O Radicals from Cavitation Bubbles under Ultrasound, Aug. 01, 2022, MDPI. doi: 10.3390/molecules27154788.
[75] K. Yasui, T. Tuziuti, Y. Iida, "Optimum bubble temperature for the sonochemical production of oxidants," in Ultrasonics, Apr. 2004, pp. 579–584. doi: 10.1016/j.ultras.2003.12.005.
[76] C. Kalmár, T. Turányi, I.G. Zsély, M. Papp, F. Hegedűs, The importance of chemical mechanisms in sonochemical modelling, Ultrason. Sonochem. 83 (Feb. 2022), https://doi.org/10.1016/j.ultsonch.2022.105925.
[77] R.E. Apfel, Acoustic cavitation prediction, J. Acoust. Soc. Am. 69 (6) (1981) 1624–1633, https://doi.org/10.1121/1.385939.
[78] C.K. Holland, R.E. Apfel, An improved theory for the prediction of microcavitation thresholds, IEEE Trans. Ultrason. Ferroelectr. Freq. Control 36 (2) (1989) 204–208, https://doi.org/10.1109/58.19152.
[79] S. Hong, G. Son, Numerical modelling of acoustic cavitation threshold in water with non-condensable bubble nuclei, Ultrason. Sonochem. 83 (Feb. 2022), https://doi.org/10.1016/j.ultsonch.2022.105932.
[80] E.A. Neppiras, Acoustic cavitation, Phys. Rep. 61 (3) (1980) 159–251, https://doi.org/10.1016/0370-1573(80)90115-5.
[81] A. J. Sojahrood, H. Haghi, R. Karshafian, and M. C. Kolios, "Classification of the major nonlinear regimes of oscillations, oscillation properties, and mechanisms of wave energy dissipation in the nonlinear oscillations of coated and uncoated bubbles," Physics of Fluids, vol. 33, no. 1, Jan. 2021, doi: 10.1063/5.0032766.
[82] A.J. Sojahrood, Q. Li, H. Haghi, R. Karshafian, T.M. Porter, M.C. Kolios, Probing the pressure dependence of sound speed and attenuation in bubbly media: Experimental observations, a theoretical model and numerical calculations, Ultrason. Sonochem. 95 (May 2023), https://doi.org/10.1016/j.ultsonch.2023.106319.
[83] F. Jaeger, O. K. Matar, and E. A. Müller, "Bulk viscosity of molecular fluids," Journal of Chemical Physics, vol. 148, no. 17, May 2018, doi: 10.1063/1.5022752.
[84] F.J. Trujillo, A strict formulation of a nonlinear Helmholtz equation for the propagation of sound in bubbly liquids. Part I: Theory and validation at low acoustic pressure amplitudes, Ultrason. Sonochem. 47 (September) (2018) 75–98, https://doi.org/10.1016/j.ultsonch.2018.04.014.
[85] O. Louisnard, I. Garcia-Vargas, "Simulation of sonoreators accounting for dissipated power", in Energy Aspects of Acoustic Cavitation and Sonochemistry, Fundamentals and Engineering, Elsevier (2022) 219–249, https://doi.org/10.1016/B978-0-323-91937-1.00021-9.
[86] O. Louisnard, J. Gonzalez-Garcia, I. Tudela, J. Klima, V. Saez, Y. Vargas-Hernandez, FEM simulation of a sono-reactor accounting for vibrations of the boundaries, Ultrason. Sonochem. 16 (2) (2009) 250–259, https://doi.org/10.1016/j.ultsonch.2008.07.008.
[87] COMSOL, "The Acoustics Module User's Guide." Accessed: Jul. 24, 2023. [Online]. Available: https://doc. comsol.com/5.4/doc/com.comsol.help.aco/AcousticsModuleUsersGuide.pdf.
[88] COMSOL, "The Structural Mechanics Module User's Guide." Accessed: Jul. 24, 2023. [Online]. Available: https://doc.comsol.com/5.4/doc/com.comsol.help.sme/StructuralMechanicsModuleUsersGuide.pdf.

[89] W.L. Nyborg, Acoustic Streaming due to Attenuated Plane Waves, J. Acoust. Soc. Am. 25 (1) (1953) 68–75, https://doi.org/10.1121/1.1907010.
[90] A.J. Reddy, A.J. Szeri, Coupled dynamics of translation and collapse of acoustically driven microbubbles, J. Acoust. Soc. Am. 112 (4) (Oct. 2002) 1346–1352, https://doi.org/10.1121/1.1502899.
[91] D. Krefting, J.O. Toilliez, A.J. Szeri, R. Mettin, W. Lauterborn, Translation of bubbles subject to weak acoustic forcing and error in decoupling from volume oscillations, J. Acoust. Soc. Am. 120 (2) (Aug. 2006) 670–675, https://doi.org/10.1121/1.2214132.
[92] J.O. Toilliez, A.J. Szeri, Optimized translation of microbubbles driven by acoustic fields, J. Acoust. Soc. Am. 123 (4) (Apr. 2008) 1916–1930, https://doi.org/10.1121/1.2887413.
[93] COMSOL, "Heat Transfer Module User's Guide." Accessed: Jul. 24, 2023. [Online]. Available: https://doc.comsol.com/5.4/doc/com.comsol.help.heat/HeatTransferModuleUsersGuide.pdf.
[94] The Engineering Toolbox, "Water - Thermal Conductivity vs. Temperature." Accessed: Aug. 11, 2023. [Online]. Available: https://www.engineeringtoolbox.com/water-liquid-gas-thermal-conductivity-temperature-pressure-d_2012.html.
[95] D. Cabaleiro, S. Hamze, J. Fal, M.A. Marcos, P. Estellé, G. Żyła, Thermal and physical characterization of PEG phase change materials enhanced by carbon-based nanoparticles, Nanomaterials 10 (6) (Jun. 2020) 1–24, https://doi.org/10.3390/nano10061168.
[96] G. Merenyi, J.S. Lind, Role of a peroxide intermediate in the chemiluminescence of luminol. A mechanistic study, J. Am. Chem. Soc. 102 (18) (Aug. 1980) 5830–5835, https://doi.org/10.1021/ja00538a022.
[97] COMSOL, "The Chemical Reaction Engineering Module User's Guide." Accessed: Jul. 24, 2023. [Online]. Available: https://doc.comsol.com/5.4/doc/com.comsol.help.chem/ChemicalReactionEngineeringModuleUsersGuide.pdf.
[98] C.T. Butts, R.W. Martin, Bayesian estimation of the hydroxyl radical diffusion coefficient at low temperature and high pressure from atomistic molecular dynamics, J. Chem. Phys. 155 (19) (2021) Nov, https://doi.org/10.1063/5.0064995.
[99] S. Uehara, H. Nikjoo, Monte Carlo simulation of water radiolysis for low-energy charged particles, J. Radiat. Res. 47 (1) (2006) 69–81, https://doi.org/10.1269/jrr.47.69.
[100] J. Wang, Y. Lai, M. Chen, Z. Jiang, G. Chen, Kinetics of luminol sonochemiluminescence quenched by purines, Luminescence 28 (2) (Mar. 2013) 102–107, https://doi.org/10.1002/bio.2345.
[101] B.A. Corzo, M.F. Suárez-Herrera, Effect of carbon tetrachloride on the luminol sonochemiluminescence reaction kinetics during multibubble cavitation, Ultrason. Sonochem. 48 (Nov. 2018) 281–286, https://doi.org/10.1016/j.ultsonch.2018.06.005.
[102] K. Yasui, Fundamentals of acoustic cavitation and sonochemistry, in: Theoretical and Experimental Sonochemistry Involving Inorganic Systems, Springer, Netherlands, 2011, pp. 1–29, https://doi.org/10.1007/978-90-481-3887-6_1.
[103] K.S. Suslick et al., Acoustic cavitation and its chemical consequences, Philos. Trans.: Math. Phys. Eng. Sci., 357(1751) (1999), 335–353. [Online]. Available: http://www.jstor.org/stable/55003.
[104] V. Salinas, Y. Vargas, O. Louisnard, L. Gaete, Influence of the liquid viscosity on the formation of bubble structures in a 20 kHz field, Ultrason. Sonochem. 22 (2015) 227–234, https://doi.org/10.1016/j.ultsonch.2014.07.007.
[105] A. Bampouli, Q. Goris, M.N. Hussain, O. Louisnard, G.D. Stefanidis, T. Van Gerven, Importance of design and operating parameters in a sonication system for viscous solutions: effects of input power, horn tip diameter and reactor capacity, Chemical Engineering and Processing - Process Intensification 198 (Apr. 2024), https://doi.org/10.1016/j.cep.2024.109715.
[106] M. Rahimi, S. Movahedirad, S. Shahhosseini, CFD study of the flow pattern in an ultrasonic horn reactor: Introducing a realistic vibrating boundary condition, Ultrason. Sonochem. 35 (Mar. 2017) 359–374, https://doi.org/10.1016/j.ultsonch.2016.10.014.
[107] I. Garcia-Vargas, O. Louisnard, L. Barthe, Extensive investigation of geometric effects in sonoreactors: Analysis by luminol mapping and comparison with numerical predictions, Ultrason. Sonochem. 99 (Oct. 2023), https://doi.org/10.1016/j.ultsonch.2023.106542.
[108] L. Yusuf, M.D. Symes, P. Prentice, Characterising the cavitation activity generated by an ultrasonic horn at varying tip-vibration amplitudes, Ultrason. Sonochem. 70 (Jan. 2021), https://doi.org/10.1016/j.ultsonch.2020.105273.